Utrecht University

Koninklijk Nederlands Meteorologisch Instituut
Ministerie van Infrastructuur en Waterstaat

Exploring the dynamics and impacts of the propagation velocity of atmospheric blocking: A model study from a Lagrangian perspective

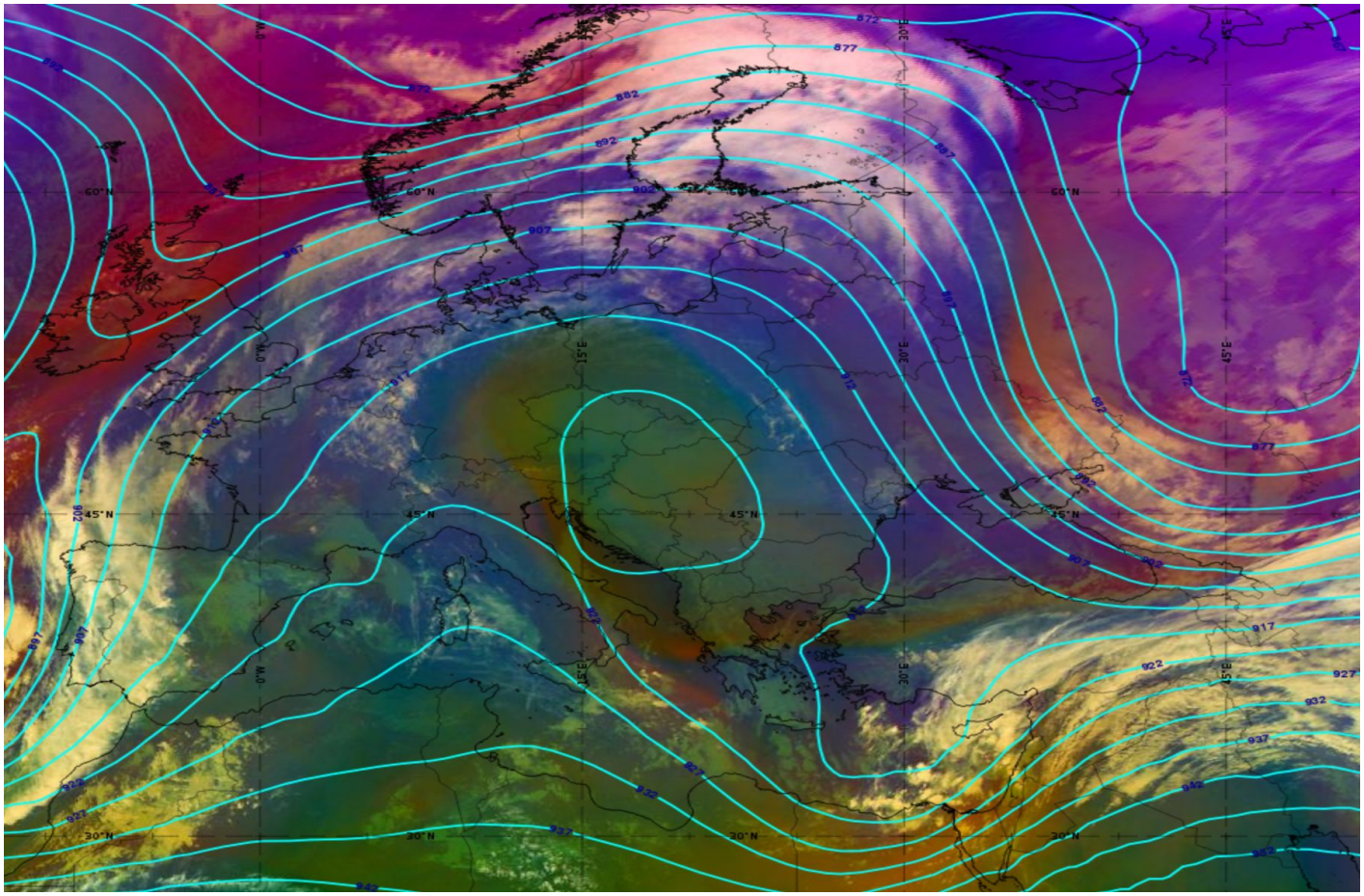

Faculty of Science

Master Thesis

Jonna van Mourik

Climate Physics

Supervisors:

Dr. H. de Vries
KNMI

Dr. M.L.J. Baatsen
IMAU

Dr. A.J. van Delden
IMAU

June 2023

Abstract

In the mid-latitudes, the prevailing westerly flow plays a crucial role in regulating weather patterns. However, this westerly flow can be disrupted by the presence of a large high-pressure area, leading to significant deviations from its original track. Such disruptions can have profound and long lasting effects on our weather, as they are associated with longer periods of drought, extreme precipitation, heatwaves, and cold spells. This disruptive weather system is commonly referred to as an atmospheric block. Due to the high impact a block can generate, atmospheric blocking has been studied extensively, but some challenges remain. The dynamics governing the formation and behaviour of blocks are not yet fully understood, resulting in difficulties for climate models to accurately simulate them. In this study, we contribute to the understanding of the dynamics of atmospheric blocking by adopting a Lagrangian framework that enables the tracking of blocks in space and time. By combining a blocking index based on geopotential height with a celltracking algorithm, we investigate the performance of the EC-Earth3$_{p5}$ climate model compared to ERA5 reanalysis data. The findings indicate that EC-Earth3$_{p5}$ generally performs well in simulating blocking behaviour, with the exception of summer blocking frequency. Within the EC-Earth3$_{p5}$ model, we observe that atmospheric blocking portrays a large variety of propagation velocities. Distinct differences are observed between the behaviour of eastward-moving blocks and westward-moving blocks. Comparing the propagation velocity with other blocking characteristics, we discover that the relation between the size and the propagation velocity resembles the Rossby wave theory. Larger sized blocks are associated with westward moving blocks, while smaller sized blocks are associated with eastward-moving blocks. In contrast, longer duration and higher intensity are associated with more stationary blocks. Although the size of atmospheric blocks is of bigger importance for the temperature anomalies, the propagation velocity has an influence on the strength of the temperature anomalies in winter, due to the slower mechanism of air advection in winter, compared to diabatic heating in summer. In summer, the propagation velocity primarily influences the positioning of temperature anomalies relative to the centre of the blocking system. These findings highlight the complex interactions between size, propagation velocity, and other blocking attributes, and their influence on temperature anomalies. Further research is warranted to explore the regional differences in blocking behavior and investigate how atmospheric blocks and their temperature anomalies may evolve under future climate conditions.

Titlepage Figure: EUMeTrain, Meteosat-11 Airmass RGB image, overlaid with 300 hPa height, for 25 November 2022 15:00 UTC.

Contents

1 Introduction **1**

2 Data and Methods **6**
2.1 EC-Earth3$_{p5}$ Model . . . 6
2.1.1 Background . . . 6
2.1.2 Model configuration . . . 6
2.1.3 Retuned parameters in EC-Earth3$_{p5}$ . . . 8
2.1.4 Selected data . . . 9
2.2 ERA5 Reanalysis . . . 10
2.2.1 Background and configuration . . . 10
2.2.2 Selected data . . . 10
2.3 Blocking Index . . . 10
2.3.1 Different indices . . . 10
2.3.2 Blocking index based on geopotential height . . . 10
2.4 2D Celltracking Algorithm . . . 13
2.4.1 The algorithm . . . 13
2.4.2 Tracking output . . . 13

3 Results **15**
3.1 Evaluation of the performance of ECE3p5 compared to ERA5 . . . 15
3.1.1 Blocking Frequency . . . 15
3.1.2 Blocking Intensity . . . 16
3.1.3 Intramodel variance . . . 17
3.1.4 Lagrangian blocking characteristics . . . 18
3.2 Characteristics of the propagation velocity of blocking in ECE3p5 . . . 19
3.2.1 Seasonality . . . 20
3.2.2 Relation between propagation velocity and other characteristics . . . 22
3.2.3 Spatial distribution of different blocking velocities . . . 24
3.3 Influence of the propagation velocity on temperature in ECE3p5 . . . 25
3.3.1 Relation between temperature anomaly and the propagation velocity . . . 25
3.3.2 Dependence of the temperature anomaly on blocking size and propagation velocity . . . 27

4 Discussion **30**
4.1 Model biases . . . 30
4.2 Choice of blocking index . . . 30
4.3 Other simplifications . . . 32

5 Conclusion **34**

A Annual mean Z500 **37**

B Seasonality of the propagation velocity over the years **38**

C Temperature anomalies associated with the propagation velocity **39**

D Temperature anomalies with respect to the blocking centre **42**

References **III**

1 Introduction

In the summer of 2018, Europe suffered from two heatwaves covering the months of July and August. In the Netherlands, this resulted in the warmest summer of the last three centuries, with a mean summer temperature of 18.9°C compared to the long-term mean value of 17.0°C (1981-2010) (KNMI 2018). These record-breaking temperatures led to wildfires, poisonous water due to algae blooms, and loss of agricultural production (World Meteorological Organization 2018). The situation was in stark contrast to the situation earlier that year, when a cold spell resulted in widespread disruption throughout Europe, even leading to the nickname of "The Beast from the East" in the United Kingdom (Guardian 2018). Despite their differences, these two temperature extremes are both linked to the same atmospheric process called atmospheric blocking (Li et al. 2020; Kautz, Polichtchouk, et al. 2020).

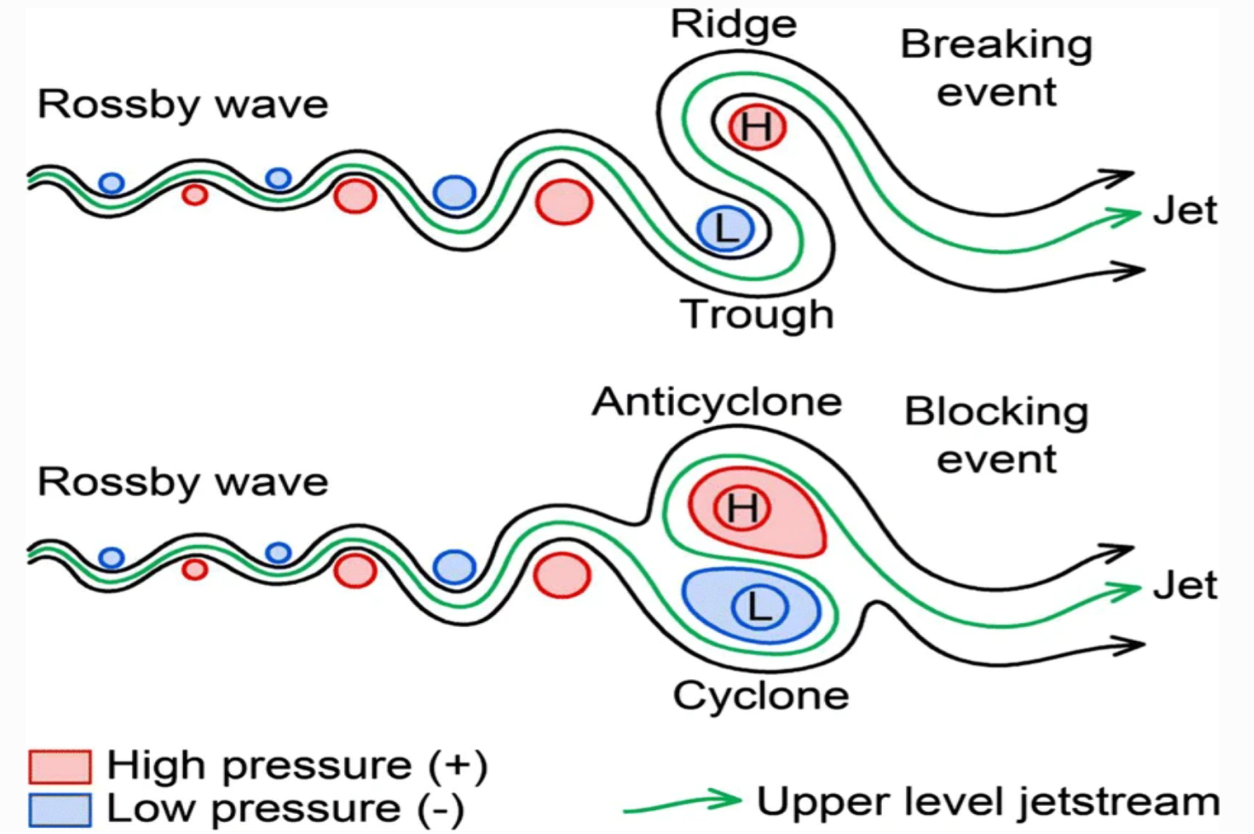

Figure 1: Schematic 2-D projection of a Rossby wave, upper level jet stream, and cyclonic breaking wave to produce an atmospheric blocking event. Taken from Mansouri Daneshvar and Freund (2019).

Atmospheric blocking is a large-scale atmospheric process, where a persistent meandering Rossby wave causes a strong high-pressure area to remain in place (Rex 1950a; Rex 1950b; Platzman 1968; Altenhoff et al. 2008). Rossby waves, or planetary waves, are potential vorticity (PV) conserving waves that exist in rotating fluids such as the atmosphere or the ocean. In the atmosphere, they depend on the variation of the Coriolis parameter with latitude. This latitudinal variation results in a meridional gradient of potential vorticity, which acts as a restoring force for meridional displacements of the Rossby wave. This process is illustrated in Figure 1, where at the top a breaking Rossby wave is shown, resulting in an omega shape blocking event, while at the bottom the growing wave leads to a dipole block, often referred to as a Rex block. The phase speed that follows from these displacements is westward with respect to the mean flow:

$$c = \frac{\omega}{k} = \bar{U} - \frac{\beta}{l^2 + k^2}. \tag{1.1}$$

In Equation 1.1, c is the phase speed, ω the frequency, and $\bar{U}$ is the mean flow, which is generally eastward in the mid-latitudes on the Northern Hemisphere. $\beta = \frac{2\Omega}{R}\cos(\phi)$ holds the rotation of the Earth Ω, the latitude ϕ, and the radius of the Earth R, and l^2 and k^2 are the meridional and zonal wavenumbers. The group velocity can be deduced from the phase velocity as

$$c_g = \frac{\partial \omega}{\partial k} = \bar{U} - \frac{\beta(k^2 - l^2)}{(k^2 + l^2)^2}. \tag{1.2}$$

c_g is positive for larger wavenumbers and negative for smaller wavenumbers, which means that smaller Rossby waves propagate eastward while larger Rossby waves propagate westward (Holton and Hakim 2013). When the these waves grow in size, they create favourable conditions for blocking formation. However, due to the complex dynamics involved in the blocking onset, multiple factors can contribute to its formation (Kautz, Martius, et al. 2022). Orography and land-sea contrasts have long been named as important contributors to blocking formation (Ji and Tibaldi 1983). More recently, the release of latent heat during cloud formation has been evaluated (Pfahl et al. 2015). After the blocking onset, blocking maintenance is needed for the persistent character of a block. Yamazaki and Itoh (2013) propose the selective absorption mechanism (SAM) as a contributor to the persistence of blocking, which is based on vortex-vortex interactions. By tracking synoptic eddies, they found that synoptic anticyclones are absorbed by blocking anticyclones, while synoptic cyclones are repelled by the block or absorbed by nearby cyclones. Because synoptic eddies have a high frequency, they are able to feed the block and thereby maintain it for several days. This mechanism is shown in Figure 2, where in (a) the earlier described omega shape block is shown and in (b) the dipole-type.

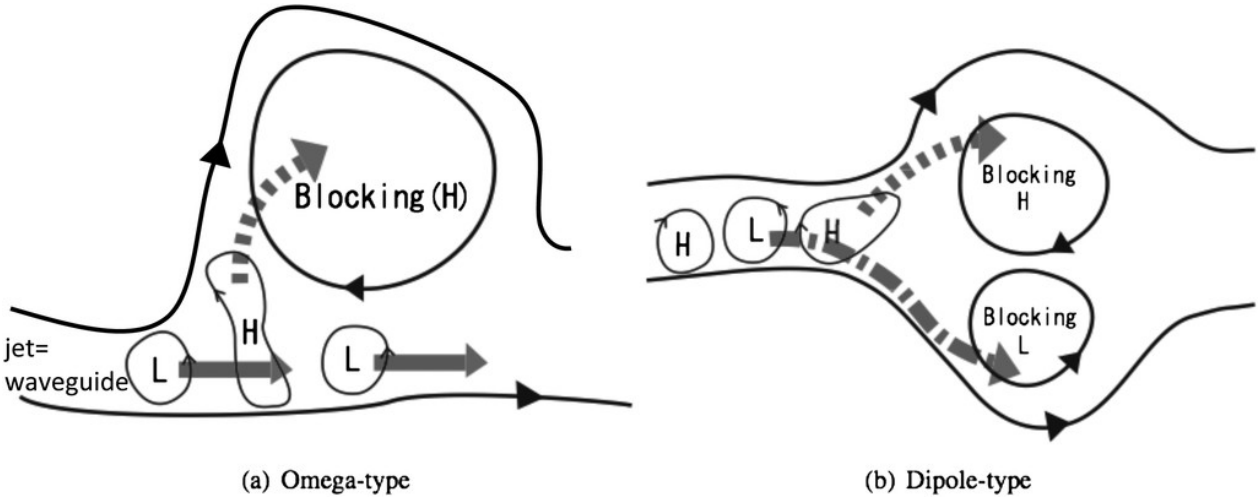

Figure 2: Conceptual diagrams illustrating the SAM. (a) For an V-type block, when synoptic eddies propagating along a waveguide approach a blocking anticyclone, synoptic anticyclones (H) are selectively absorbed by the blocking anticyclone, while synoptic cyclones (L) are repelled and drift downstream. (b) As in (a), but for a dipole-type block. Taken from Yamazaki and Itoh (2013).

Blocking is common in regions with a high storm-track activity, such as the central Pacific and the Euro-Atlantic sector, due to the advection of anticyclonic vorticity eddies. Although both these regions are located at the end of an active storm-track, their blocking patterns differ in latitude as blocking events over the Euro-Atlantic regions are located further southwards compared to blockings over the central Pacific (Barriopedro et al. 2006). Blocking also occurs further inland over the Ural region, caused either by an extended storm-track over the North Atlantic towards the Mediterranean Sea, or by an interaction of Rossby waves with the cold Siberian high (Cheung, Zhou, Shao, et al. 2013). Lastly, blocking can be observed over Greenland, where it correlates with a negative NAO-index (Davini, Cagnazzo, Neale, et al. 2012).

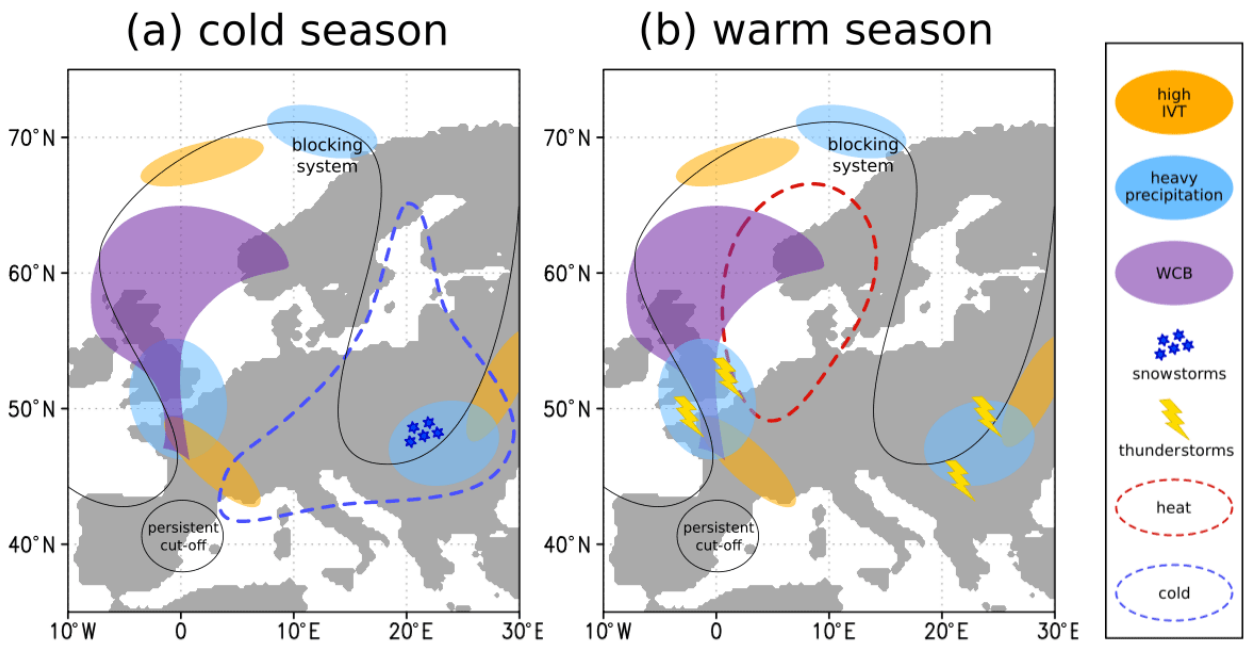

Figure 3: Schematic illustration of a blocking system (black line, indicating a geopotential height or PV contour) and some associated surface extremes during (a) the cold season (October–March) and (b) the warm season (April–September). Rossby wave breaking occurs on the flanks of the block, leading to (persistent) cutoff systems in this area. Blue stars show areas where snowstorms are observed (eastern flank of the block). Areas with heavy precipitation are marked in light blue (poleward edge of the ridge and at both flanks). Areas with high integrated water vapor transport (IVT) are illustrated in orange. Thunderstorm activity is marked by yellow lightning bolt symbols. The position of a warm conveyor belt appears in purple. Areas with temperature extremes are marked with dashed lines (red for heat waves and blue for cold spells). Taken from Kautz, Martius, et al. (2022).

The influence of blocks on our weather is significant as these blocks cover a large area, can last from days up to a month, and are quasi-stationary (Liu 1994). Nakamura and Huang (2018) use the apt analogy of an atmospheric blocking as a traffic jam in the jet stream, which therefore has to deviate from its prevailing westerly flow. This deviation is one of the drivers behind the weather extremes that can be caused by atmospheric blocking, although the effect on our weather varies from season to season. This seasonal difference is shown in Figure 3, where in (a) the winter season and in (b) the summer season is shown under influence of an imaginary omega blocking condition. Atmospheric blocking in winter is mostly associated with cold spells. These cold spells often form downstream of the block, as is depicted with the blue dashed line in Figure 3a. Upstream of the block, a warm conveyor forms with warm air and moist conditions. Both these upstream and downstream processes are caused by horizontal advection of respectively warm air from the tropics and cold air from the polar regions, driven by the high-pressure area (Bieli, Pfahl, and Wernli 2015). Besides the advection by the blocking high, the deviation of cyclones also plays an important role in determining the exact locations of cold and warm anomalies (Kautz, Martius, et al. 2022). In the case of blocking over land, another process that favours the formation of cold spells is subsidence below the anticyclone. This subsidence generally leads to cloud-free conditions, which in winter results in an increase in outgoing long-wave radiation and hence further cooling (diabatic cooling). Simultaneously, subsidence leads to adiabatic heating as the descending air is compressed and warms. Taken together, subsidence can lead to opposing warming and cooling. However, the effects of both adiabatic heating and diabatic cooling are of secondary importance compared to the influence of horizontal advection in winter (Sousa, Trigo, et al. 2017). As this horizontal advection is a much slower process compared to both diabatic cooling and adiabatic heating, Brunner, Hegerl, and Steiner (2017) showed that cold spells take a longer period of time to develop. In addition to the blocking effect on temperature, precipitation is also affected. In Figure 3a, heavy precipitation is shown in light blue

and areas with a high integrated water vapour transport are shown in orange. These areas are found at the boundaries of the block, where the blocking high forms fronts with bypassing cyclones (Rex 1950a). In contrast, anomalously dry conditions are found underneath the block. These dry conditions are caused by the earlier mentioned process of subsidence, leading to cloud-free conditions and thus an absence of precipitation. For the combination of these processes of subsidence and cyclone deflection, the type of blocking is important. Omega blocking results in dry conditions both south of the block and below it, with increased precipitation at the other outer edges, whereas Rex blocking results in dry conditions underneath it and increased precipitation to the south due to a more active southerly displaced jet stream (Sousa, Barriopedro, et al. 2021). Due to the cold temperatures, positive precipitation anomalies can also come in the form of snowstorms, as is indicated in Figure 3a with dark blue stars.

Summer blocking is mostly associated with the build-up of heatwaves and droughts. These heatwaves are accounted for by the same physical principles as in winter, but their outcome is notably different, just as their order or importance. Just as in winter, horizontal advection leads to the influx of colder air from higher latitudes and warmer air from lower latitudes. While this was the main contributor to temperature anomalies in winter, this is not the case in summer, where subsidence plays the dominant role. Especially during the day, adiabatic warming and diabatic warming due to subsidence reinforce each other and result in positive temperature anomalies (Röthlisberger and Martius 2019; Bieli, Pfahl, and Wernli 2015). Only at night, the cloud-free conditions lead to an increase in outgoing long-wave radiation and thus diabatic cooling, which suppresses the daily mean temperatures. As subsidence plays a bigger role in the realisation of higher temperatures, these temperatures are found right underneath the block, as is shown in Figure 3b. In Rex-type blocking (see Figure 1, lower panel), these positive temperature anomalies often co-occur with negative temperature anomalies to the south of the block, due its dipole-pattern with a cyclone under the block (Sousa, Trigo, et al. 2017). The dynamics leading to positive and negative precipitation anomalies are the same for winter and summer. Underneath the block however, land-atmosphere interactions become more important in summer. Due to the higher temperatures and dry conditions below the block, the dry soil enhances the surface sensible heat-flux, which in turn can contribute to the intensity of the block (Schumacher et al. 2019). A last notable difference between winter and summer blocks is the formation of thunderstorms in summer. These thunderstorms can form due to the collision of stable, convection-inhibiting air underneath the block with warm, moist, unstable and thus convection-favouring air at the flanks of the block (Mohr et al. 2019), and are illustrated with yellow lightning bolt symbols in Figure 3b.

Atmospheric blocking has been a subject of research for over a century because of the high impact weather we just described(Garriott 1904), but it was not until 1950 that Rex (1950a) first proposed its definition. Since then, scientists have been trying to understand different blocking characteristics that attribute to the impact of blocks on our weather, such as their size (Nabizadeh et al. 2019), intensity (Wiedenmann et al. 2002; Davini, Cagnazzo, Gualdi, et al. 2012), duration (Barnes, Slingo, and Woollings 2012) and location(Brunner, Schaller, et al. 2018; Sousa, Trigo, et al. 2017). A lot of attention has also been given to the seasonality of blocking characteristics, such as by Tyrlis and B. Hoskins (2008), Cheung, Zhou, Mok, et al. (2013), and Lupo (2021). Research on blocking is most often conducted by performing case studies using reanalysis data (Dong et al. 2018). The use of these case studies is effective in quantifying the effects of specific blocks, but is limited by the amount of data available. This is where climate models come in as they enable bigger datasets that can enhance our comprehension of the underlying processes that drive atmospheric blocking. However, climate models are not perfect, which is why research also focuses on the assessment of model quality (Scaife et al. 2010). Over the years, climate models have massively improved in their ability to simulate atmospheric blocking, but some offsets remain compared to the reanalysis data. Especially over Western Europe blocking is underrepresented in current climate models (Davini and d'Andrea 2020). Despite the large amount of research that has already been conducted, still much of the behaviour of blockings is unknown to us.

One of the most overlooked components of atmospheric blocking is the propagation velocity of the block. The velocity component is often ignored for simplicity and it is not included in blocking indices that are used to identify blocks from datasets (Sousa, Barriopedro, et al. 2021; Pelly and Brian J Hoskins 2003). The first author that did write something about blocking propagation velocity was Sumner (1963) ((Kikuchi 1971)?) in 1963, who came up with the terms of progressive (eastward moving), quasi-stationary and retrogressive (westward moving) blockings. These categories were split by a threshold value of 5° per day in both the

eastward and westward direction, and it was found that about 40% of all blocks was quasi-stationary, 35% was progressive 25% was retrogressive for the Atlantic-European section. However, no conclusions were drawn on what this meant for our weather, and as Sumner (1963) used a minimum blocking duration of two days, these values are probably not representative for our current understanding of blocking with a minimum duration of four days. In 2018, Mokhov and Timazhev (2019) tested multiple threshold values of maximum zonal propagation velocity of blockings, where they distinguished between daily displacements of 0.5, 0.4 and 0.3 of its radius. They showed that these different threshold values led to different frequencies of blocking, but that they could all be used to assess their main research question on trends in blocking frequency. Lastly, Steinfeld et al. (2018) studied the distributions of mean zonal propagation velocity during the lifetime of blocks and concluded that this velocity was highest in their onset phase and decreased during their mature phase. They also mention that their blocking algorithm detected some blockings with propagation velocities larger than 10 m s^{-1} (864 km d^{-1}), but they doubt if they can be seen as classical blocks.

So far, no studies have considered the effect that the propagation velocity has on our weather. One of the reasons for this is probably that most studies on blocking have used an Eulerian framework, which does not permit the tracking of atmospheric blocking. However, as especially the build-up to winter temperature extremes takes time (Brunner, Hegerl, and Steiner 2017), it is plausible that blocking propagation velocities influence the impact caused by the block. Thus, we first need to gain a better understanding of this characteristic of atmospheric blocking to know whether this would lead to new insights in predicting blocking related impact. In our research, we make a first attempt to deepen this understanding using the latest update of the climate model EC-Earth3_{p5} (in short: ECE3p5) and by focusing on the northern hemisphere. Our study has three objectives: we will start with an evaluation on the performance of this model compared to ERA5 reanalys data. This is necessary to correctly interpret our results later on and will provide us with more knowledge on the climatology of atmospheric blocking in our model environment, which could be important for scenarios made by the KNMI; then, we will dive deeper in the characteristics of the zonal propagation velocity of atmospheric blocking and how it relates to blocking size, intensity, duration and location; and lastly, we will look at the influence the propagation velocity has on temperature anomalies and compare this to the influence of blocking size in order to estimate the importance of the propagation velocity of atmospheric blocking.

This thesis is build up as follows: a description of EC-Earth3_{p5} and ERA5 is given in Section 2 together with an overview of the used data-variables and the methods that were used. Our results are shown in Section 3 and discussed in Section 4. Lastly, our conclusions are summarized in Section 5.

2 Data and Methods

In this section we will elaborate on the model, the used datasets and methods that were applied to gather information on atmospheric blocking.

2.1 EC-Earth3$_{p5}$ Model

2.1.1 Background

The model that is used in this thesis is EC-Earth3$_{p5}$ (ECE3p5), which is the latest update of EC-Earth3 (ECE3). EC-Earth is short for the European Community Earth System Model and it has been developed for Earth system studies, for which complex models are needed that are able to solve not only the physics of the atmosphere, ocean, cryosphere and land, but also biophysical and biogeochemical processes. The need for models such as EC-Earth is stressed by the Paris Climate Accord, in which it was agreed to try to limit the global mean temperature to 1.5° in the time period of 2021 to 2030. One of their main pillars was "recognizing the need for an effective and progressive response to the urgent threat of climate change on the basis of the best available scientific knowledge" (Paris Agreement). Climate models play an important role in this scientific knowledge, as they make it possible to explore our world under different circumstances, such as a higher global mean temperature (Kawamiya et al. 2020).

The development of the EC-Earth model has gone through many stages, with the first version launched in 2008. The second version was included in the fifth phase of the Coupled Model Intercomparison Project (CMIP5), and the third version was included in the sixth phase (CMIP6). However, the model continues to have a number of inadequacies. One of the main shortcomings with ECE3 is its temperature bias compared to ERA5 reanalysis. In the Northern Hemisphere, ECE3 has a cold bias, while in the southern hemisphere a warm bias dominates. As the warm bias is larger than the cold bias, the model produces a warmer global mean temperature than ERA5 (Hersbach et al. 2020). Another shortcoming of ECE3 is the simulation of the Atlantic Meridional Overturning Circulation (AMOC), as the variability it produces exceeds realistic values (Döscher et al. 2022). However, solving both the cold and the warm biases simultaneously is not straightforward, so it was decided to focus the newest version of EC-Earth, ECE3p5, solely on correcting the cold bias and the variability of the AMOC in the Northern Hemisphere. The trade-off of this approach is an even larger warm bias over the Southern Hemisphere and thus also a higher global mean temperature, but with a better representation over the Northern Hemisphere (Reerink $\sim$ 2023-2024, Under review). As we are only evaluating Northern Hemispheric atmospheric blocking, ECE3p5 is the most appropriate choice for our research.

2.1.2 Model configuration

ECE3p5 is a single-model initial-condition large ensemble climate model, or SMILE for short. As the name suggests, it consists of many ensemble members, all with the same physics and forcing, but with different initial conditions. Due to the inherent chaotic nature of the Earth system, every run results in a unique simulation that takes the internal variability of our climate state into account (Muntjewerf et al. 2023). For our study, we use 16 ensemble members of 164 years, ranging from 1850 to 2014, resulting in a total dataset of 2624 years. Döscher et al. (2022) refer to this dataset as the historical period. The standard resolution is T255L91 ($\approx$ 80 km) for the atmosphere and ORCA1L75 (1°) for the ocean, and the model uses time steps of 2700 s (45 minutes).

ECE3p5 has different model components for different research areas. In total, the model is able to describe the atmosphere, ocean, sea ice, land surface, dynamic vegetation, atmospheric composition, ocean biogeochemistry, and the Greenland Ice Sheet. These different components are shown in Figure 4, together with their coupling links and typical frequencies, and the models that are responsible for the specific components. EC-Earth3$_{p5}$ is the standard configuration consisting of the atmosphere model IFS including the land surface module HTESSEL and the ocean model NEMO3.6 with the sea ice module LIM3. Next to the standard configurations, there are the options for EC-Earth3$_{p5}$-Veg for dynamic vegetation, EC-Earth3$_{p5}$-AerChem for the atmospheric composition, EC-Earth3$_{p5}$-CC that includes the dynamic vegetation, atmospheric composition, and the ocean biochemistry, and lastly EC-Earth3$_{p5}$-GrIS that includes the dynamic vegetation

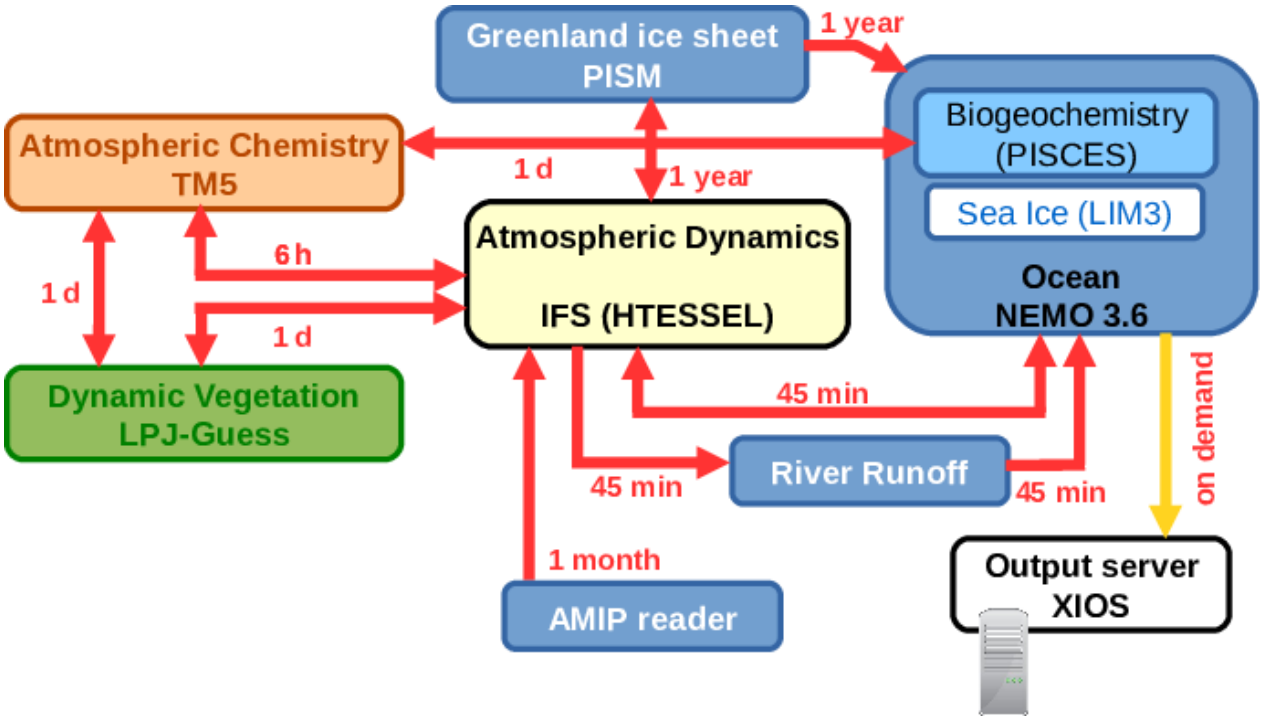

Figure 4: Coupling links and typical frequencies at standard resolution between all components that potentially can be coupled. Existing configurations include subsets of component models and associated couplings. Taken from Döscher et al. (2022).

and Greenland Ice Sheet. As our research topic revolves around atmospheric dynamics, we make use of the standard configuration. The core of this standard configuration is made up by the Integrated Forecast System (IFS) version CY36R4. This model represents all physical processes in the atmosphere that are shown in Figure 5, such as convection, radiation, heat fluxes, drag forces and precipitation by solving the hydrostatic primitive equations. All information on these equations and the physical processes involved can be found in ECMWF (2010). IFS was originally introduced for operational medium-range forecasting and therefore some alternations were needed to make it suitable for running long climate simulations (Molteni et al. 2011; Döscher et al. 2022).

The IFS model is coupled to HTESSEL, which stands for the Hydrology Tiled ECMWF Scheme of Surface Exchanges over Land. To account for different vegetation types, each gridcell is subdivided into fractions, which they call tiles. The model solves the energy and water balance at the land surface by attributing one tile to the dominant vegetation type that can be found over that area. Distinctions are made between bare ground, low and high vegetation, intercepted water by vegetation, and vegetation-shaded and exposed snow. These different surface types and therefore different tile skin temperatures result in a better representation of heat and water fluxes within the surface energy balance. It also includes surface runoff of water, for example towards rivers, which happens when the maximum infiltration rate is exceeded Balsamo et al. 2009. The output of this runoff is communicated with the coupled ocean model.

The ocean model incorporated in ECE3p5 is the Nucleus for European Modelling of the Ocean version 3.6 (NEMO3.6), which is a model intended for oceanographic research, seasonal forecasts and climate studies. It consists of the ocean model OPA (Océan Parallélisé), the LIM3 sea ice model (Louvain-la-Neuve Ice Model), and the PISCES model (Pelagic Interactions Scheme for Carbon and Ecosystems Studies), which takes the biogeochemistry into consideration. OPA accounts for the primitive equations of the ocean circulation, both on regional and global scale. These primitive equations are the Navier-Stokes equations and the equations of state for temperature and salinity and together they form the basics for the fluid dynamics in the ocean (Madec et al. 1997). Besides the freshwater runoff coming from HTESSEL, the atmosphere and the ocean also interact

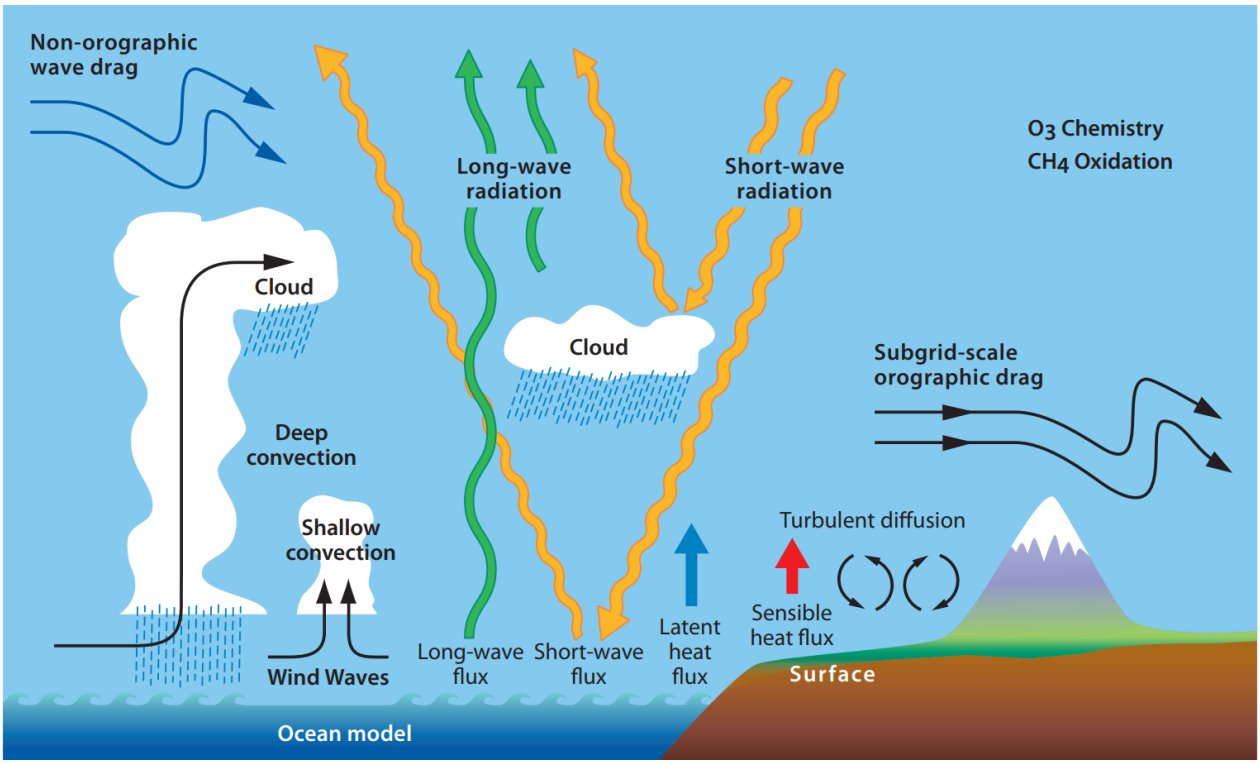

Figure 5: Schematic diagram of the different physical processes represented in the IFS model. Taken from ECMWF (2010).

directly via precipitation and evaporation, and the exchange of wind stress and heat. Sea ice is included in the ocean model via LIM3, which is based on the Arctic Ice Dynamics Joint Experiment (AIDJEX) framework (Coon, Maykut, and Pritchard 1974). A good representation of sea ice in the model is important due to its high albedo and seasonal variability, but also because of its influence on the general ocean circulations (Rousset et al. 2015). LIM3 combines multiple ice categories and their thickness distribution (Thorndike et al. 1975), halo-thermodynamics, and the conservation of horizontal momentum. Lastly, PISCES-v2 is responsible for the simulation of the nutrient cycles of nitrogen, phosphor, iron and silicon, and both the inorganic and organic carbon cycle. Part of this inorganic carbon cycle is the uptake of of atmospheric CO_2, which plays an important role in climate modulation (Aumont et al. 2015; Sabine et al. 2004). For the organic cycle, PISCES includes different types of plankton which are regulated by the nutrient cycles. Combining the physics, sea ice and biogeochemistry, NEMO3.6 gives a good approximation of the state of our ocean and its influence on our climate.

2.1.3 Retuned parameters in EC-Earth3$_{p5}$

Every simulation is characterized by a variant label consisting of the letters **r**1**i**1**p**1**f**1, where the numbers can vary. It includes the **r**ealization index, **i**nitialization index, **p**hysics index, and **f**orcing index. The realization index denotes the ensemble member that you are working with. The original EC-Earth3 model has the physics index $p1$, and the new update will have the physics index $p5$, indicating that part of the physics of the model is changed. The parameters that were retuned are the threshold for snow autoconversion and the fall speed of ice particles in clouds. Both can be found within the IFS model under the topic of clouds and large-scale precipitation (Tiedtke 1993).

The snow autoconversion threshold has an influence on the typical cloud water content at which the generation of precipitation begins to be efficient (ECMWF 2010). The larger value for the snow autoconversion threshold results in a higher cloud water content, leading to a higher amount of ice particles in high clouds. Due to this increase in ice particles, the high clouds grow in height and therefore cool down, which reduces the outgoing

longwave radiation into space and thus leads to effective warming. Another effect of increasing the threshold for snow conversion is the lower albedo of ice particles compared to water droplets, which also has a warming effect. The other tuning parameter is the terminal fall speed of cloud ice particles and it is reduced compared to ECE3. A lower fall speeds results in longer floating ice particles and extends the life time of the high clouds. As the high clouds have a longer lifetime, the amount of high clouds will increase, just as their cloud top heights, both resulting in effective warming (Reerink ∼ 2023-2024, Under review).

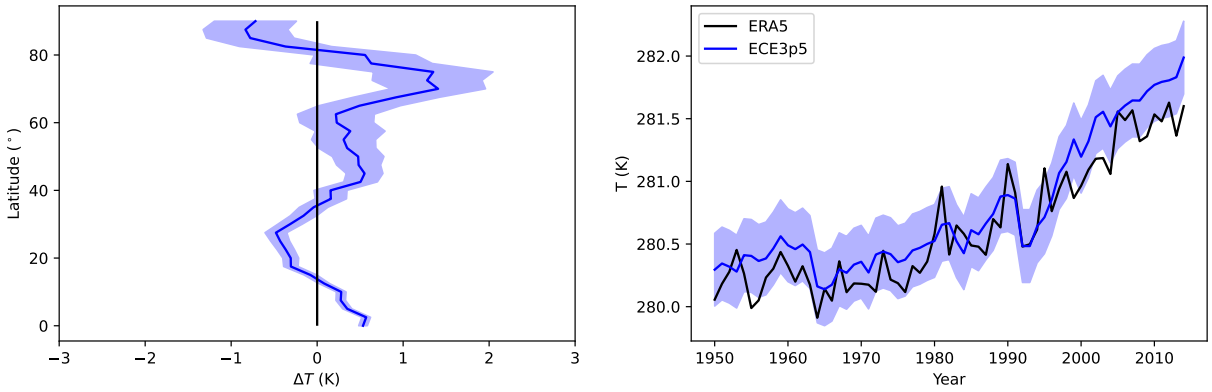

(a) NH zonal mean bias in TAS (K)

(b) NH annual mean TAS (K)

Figure 6: ECE3p5 model (blue line) temperature bias on the NH compared to ERA5 (black lines) over 1950-2014. Blue shade shows one standard deviation (σ) of the variability over the 16 ensembles in ECE3p5.

As a result, the temperature bias in the Northern Hemisphere decreases in ECE3p5, while the temperature bias in the Southern Hemisphere increases. For ECE3p5, the zonal mean model bias in the surface temperature is shown in Figure 6a. Both the positive and negative temperature bias with the reanalysis data of ERA5 stay within two degrees, whereas ECE3 only had negative zonal mean biases for the Northern Hemisphere (Döscher et al. 2022). The annual mean surface temperature for both ECE3p5 and ERA5 is shown in Figure 6b. The Northern Hemisphere annual mean surface temperature for ERA5 stays within the ensemble variability of ECE3p5, although the differences get bigger from 1995 on. From this year, the model starts to simulate larger annual mean surface temperatures than ERA5. This same discrepancy was found by Döscher et al. (2022), who noted a trend of 0.25 K/decade for the ECE3 ensemble mean, and 0.18 K/decade for ERA5. These values were found for the average of the Northern and Southern Hemisphere together over the period of 1980-2010. For the NH of ECE3p5 we found a trend of 0.45 K/decade and 0.33 K/decade for ERA5 over the same period. Both these values are larger than the ones for the Earth as a whole, showing the larger warming trend over the Northern Hemisphere.

2.1.4 Selected data

For the identification of the blocks, the geopotential height at 500 hPa (Z500) (m) is used, as will be explained in Section 2.3.2. The geopotential height gives the gravity-adjusted height above mean sea level at which a pressure of 500 hPa is measured, and we use its daily mean value. The other selected variable is the daily mean surface air temperature at 2m (TAS) (K). As we want to know the relative impact of blocks on temperature, these temperatures are detrended and corrected for climatology, leading to temperature anomalies that allow us to compare the impact on different locations and seasons. In order to capture the influence of of blocks on temperature anomalies, a tracking area with a latitude-width of 40° and a longitude-width of 80° is employed around the centre of the block. The size of the area is selected to encompass the size of the majority of the blocks, ensuring that it adequately captures the diverse range of temperature anomalies associated with them. This size is comparable with approximately a quarter of the area shown in Figure 7 below. Both variables are downloaded in their original resolution, which was mentioned in Section 2.1.2. However, as atmospheric blocking is a large scale process, we can regrid this to a regular lat-lon grid of 2.5° × 2.5° using bilinear interpolation.

2.2 ERA5 Reanalysis

2.2.1 Background and configuration

To asses the ability of EC-Earth3$_{p5}$ to simulate atmospheric blocking, we compare it with the ERA5 reanalysis dataset from ECMWF (1950-2022). ERA5 is the successor of ERA-Interim and it combines model data from IFS Cy41r2, which is the version of 2016, with observations to gain a globally complete dataset via data-assimilation. These observations are gathered from satellite instruments combined with in-situ measurements, such as at land stations, drifting buoys in the ocean, radiosondes, balloon observations and aircraft-based atmospheric observations. In total, this leads to a data-influx of 0.75 million observations per day (measured in 2019). To couple all this data, data-assimilation is used with the objective to find the best estimate of the state of the atmosphere. For the data-assimilation, 4D-Var, a four-dimensional variational data assimilation system is used.

2.2.2 Selected data

From this dataset, we only use the daily mean geopotential at 500 hPa (m^2s^{-2}), which can be transformed to the geopotential height by dividing it by the Earth's gravitational acceleration (Copernicus Climate Change Service 2023). ERA5 has a resolution of $0.25° \times 0.25°$ (Hersbach et al. 2020), but in order to comply with our regridded dataset from EC-Earth3$_{p5}$, we regrid the $0.25° \times 0.25°$ grid of ERA5 to $2.5° \times 2.5°$.

2.3 Blocking Index

2.3.1 Different indices

Since Rex (1950a) first introduced a definition of atmospheric blocking, multiple different blocking indices have emerged to extract these blocks from datasets. They differ in the dynamical aspects of a block that they grasp, but also in the minimal duration, size or location of a block, or in their dimension as some only capture one dimensional aspects while others caption multiple dimensions. As a result, it is difficult to compare different studies on blockings (Sousa, Barriopedro, et al. 2021; Barnes, Dunn-Sigouin, et al. 2014). Two of the most used indices are the ones by Pelly and Brian J Hoskins (2003), who propose a dynamical framework to look at blocking by considering potential temperature (θ) on a constant potential vorticity surface, and by Stefano Tibaldi and Molteni (1990), using the geopotential height gradient at 500 hPa. Both have been updated by other authors over the years, leading to even more discrepancies between studies (Pinheiro, Ullrich, and Grotjahn 2019). The main advantage of working with the PV-index is that it is based on dynamical features, which makes it possible to track blockings in time and is used to determine its size over its lifetime and its longevity. It is thus a Lagrangian way of looking at blockings. This is an important aspect that is missing in the geopotential height-index, which works from the Eulerian framework. This Eulerian framework is often used to determine the impact of atmospheric blocking on our weather, since for this it is only important how long a block remains over a certain area. Another factor to consider is that whereas the geopotential height is a standard output of both the ECE3p5 model and the ERA5 reanalysis, the PV-analysis depends on a vertical integration, resulting in the need of a lot more model data. Because we have access to a 2D celltracking algorithm, which we will discuss in more detail in Section 2.4, we have the ability to transform the geopotential height-index into a Lagrangian framework and thus track the blocks in time, which is necessary if we want to study blocking propagation. This removes the main disadvantage of the geopotential height-index compared to the PV-index. Combined with the accessibility of the geopotential height in our model data, we decided to work with the geopotential height-index, which will be described in more detail below. A discussion of how our chosen blocking index influences our results compared to other studies can be found in Section 4.

2.3.2 Blocking index based on geopotential height

The blocking index that we use here, is based on the geopotential height-index of Stefano Tibaldi and Molteni (1990) and takes the majority of the alterations of Sousa, Barriopedro, et al. (2021) into account, which are meant to make the blocking index more inclusive and precise. The method to get from the geopotential height to an identified block is explained here and shown in Figure 7.

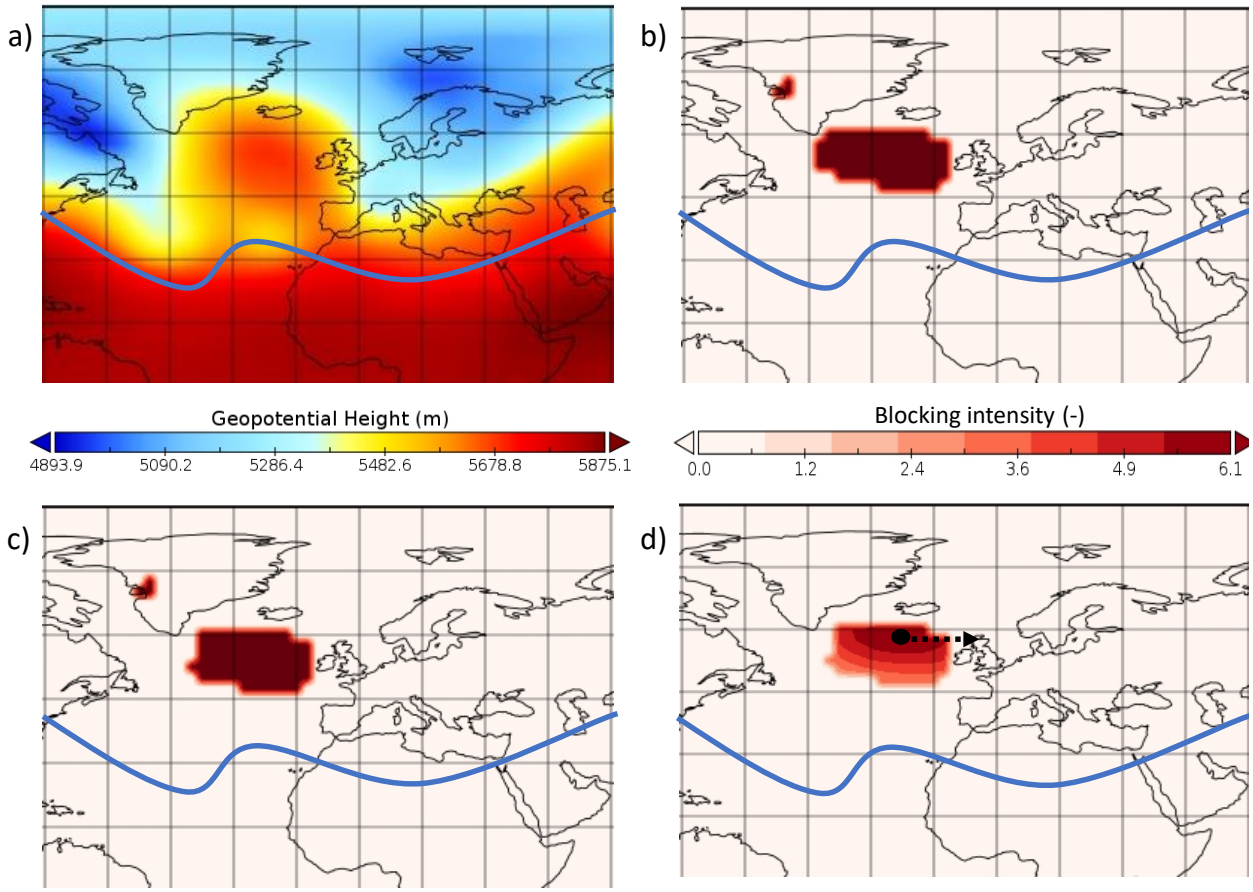

Figure 7: a) Geopotential height map of an arbitrary block. b) Filter for regions where GHGS$>$ 0 and GHGN$<$ 0. Index is either 0 or 1. c) Filter for regions where GHG$<$ 20 m per degree. Index is either 0 or 1. d) Add blocking intensity and track the block; remove blocks with an area smaller than 500.000 km^2 and of shorter duration than 4 days. For all subfigures, the blue line represents an approximation of the minimum latitude LAT$_{min}$.

The first step of this method is the exclusion of the subtropical high pressure belt from our blocking analysis. Because the onset of atmospheric blocking is often preceded by a subtropical ridge which is attached to the subtropical high pressure belt, a distinction needs to be made to only include the ridges in the analysis. Sousa, Barriopedro, et al. (2021) defines the subtropical belt as areas where the instantaneous local geopotential height at 500hPa (Z500) is higher than the hemisphere-wide (area-weighted) mean Z500 averaged over the previous 15 days. This leads to the condition

$$Z500(\lambda, \phi, d) > \overline{[Z500]}, \tag{2.1}$$

where λ is the longitude, ϕ is the latitude, d is the day, the square brackets denote the spatial mean, and the overbar the time mean. The lowest latitude for which the condition of Equation 2.2 is satisfied, is called the minimum latitude LAT$_{min}$. The blocking analysis will only be executed above this latitude to exclude the subtropical high pressure area from the analysis. This is illustrated in Figure 7a. As the location of the subtropical high depends on the position of the sun and thus on the seasons, the minimum latitude is found further poleward in summer compared to winter. Sousa, Barriopedro, et al. (2021) calculates one value for LAT$_{min}$ for each day, by averaging over all longitudes. However, as these minimum latitudes differ over different regions over the earth, we chose to use a longitude dependent minimum latitude:

$$Z500(\lambda, \phi, d) > \overline{Z500}. \tag{2.2}$$

Especially over the Euro-Atlantic region in winter this makes a difference, since the longitude dependent LAT_{min} is situated 7.5° further poleward than the longitude averaged LAT_{min}. This can be seen in Figure 8.

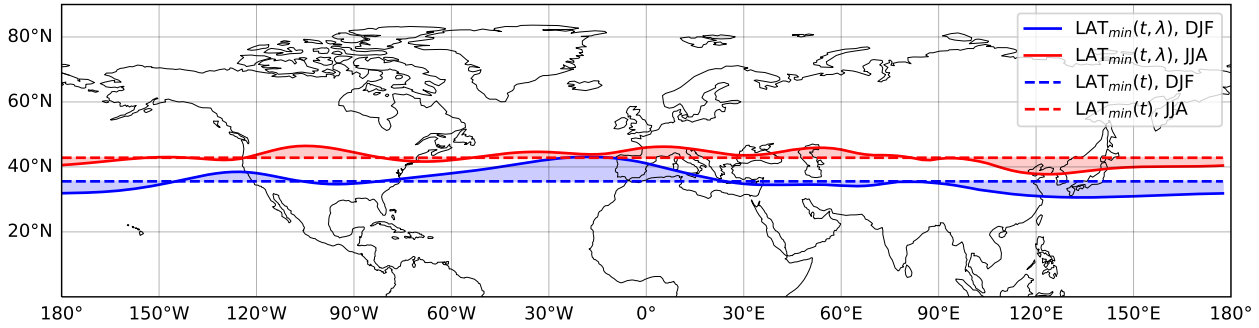

Figure 8: Difference between the latitude dependent minimum latitude $\mathrm{LAT}_{min}(t,\lambda)$ (continuous line) and the spatial averaged minimum latitude $\mathrm{LAT}_{min}(t)$ (dashed line), both for winter (DJF, blue) and summer (JJA, red).

For this blocking analysis, a gridpoint is said to be blocked if at the same time equatorward easterlies (GHGS> 0) and poleward westerlies (GHGN< 0) are true with respect to the gridpoint. Together, they indicate the meridional flow reversal associated with atmospheric blocking. In formulas, this translates to the geopotential height gradients

$$\mathrm{GHGS}(\lambda,\phi,d) = \frac{[Z500(\lambda,\phi,d) - Z500(\lambda,\phi-\Delta\phi,d)]}{\Delta\phi} \text{ if } \mathrm{LAT}_{min} \leq \phi, \tag{2.3}$$

and

$$\mathrm{GHGN}(\lambda,\phi,d) = \frac{[Z500(\lambda,\phi+\Delta\phi,d) - Z500(\lambda,\phi,d)]}{\Delta\phi} \text{ if } \mathrm{LAT}_{min} \leq \phi \leq 75°, \tag{2.4}$$

where $\Delta\phi = 15°$. Due to this value of $\Delta\phi$, GHGN is undefined poleward of 75°. The result of this filter is shown in Figure 7b. To ensure that the jet is not included in the block, strong winds are excluded based on the zonal and meridional Z500 gradients, which together represent a local measure of the geostrophic wind magnitude. This measure consists of a zonal (Equation 2.5) and a meridional component (Equation 2.6), which together form the geopotential height gradient (Equation 2.7). Whenever this geopotential height gradient is bigger than 20 m per degree latitude, the area is marked as a strong wind area and left out of the analysis, as is shown in Figure 7c.

$$\mathrm{GHG}_z = \frac{Z500(\lambda,\phi+\Delta\phi,d) - Z500(\lambda,\phi-\Delta\phi,d))}{2\Delta\phi} \tag{2.5}$$

$$\mathrm{GHG}_m = \frac{Z500(\lambda+\Delta\lambda,\phi,d) - Z500(\lambda-\Delta\lambda,\phi,d))}{2\Delta\lambda} \tag{2.6}$$

$$\mathrm{GHG}(\lambda,\phi,d) = \sqrt{{\mathrm{GHG}_z}^2 + {\mathrm{GHG}_m}^2} < 20\text{m per degree.} \tag{2.7}$$

In Equation 2.5 and 2.6 the $\Delta\phi$ and $\Delta\lambda$ both have values of 2.5°, as this is the resolution that we have chosen for our grid. The last step in which we follow Sousa, Barriopedro, et al. (2021), is the exclusion of blocks smaller than 500000 km^2 and of shorter duration than 4 days, which is done after using the tracking algorithm explained in Section 2.4. While Sousa, Barriopedro, et al. (2021) continues with the deviation between different types of blocks, we evaluate them together and add a blocking intensity based on Wiedenmann et al. (2002). Davini, Cagnazzo, Gualdi, et al. (2012) slightly modified this method to be two-dimensional, which resulted in

$$\mathrm{RC}(\lambda,\phi,d) \equiv \frac{(Z_u + Z500(\lambda,\phi,d))/2 + (Z_d + Z500(\lambda,\phi,d))/2}{2\phi}$$

$$\mathrm{BI}(\lambda, \phi, d) = 100[\frac{Z500(\lambda, \phi, d)}{\mathrm{RC}} - 1.0]. \tag{2.8}$$

In Equation 2.8, RC stands for representative contour, Z_u is the minimum value within 60° upstream of a value Z500 and Z_d is the minimum value within 60° downstream of this same Z500. The value resulting from it, determines the blocking intensity and indicates how the meridional circulation is affected by the presence of the block. According to Wiedenmann et al. (2002), blocks on the Northern Hemisphere are weak when they have a value of BI< 2.0, moderate when 2.0 <BI< 4.3 and strong when BI> 4.3. They based their categorisation on which blocks were within and outside of one standard deviation of the 30-year mean intensity of their dataset. For our example block, this is shown in Figure 7d.

2.4 2D Celltracking Algorithm

2.4.1 The algorithm

As we want to evaluate the propagation velocity of atmospheric blocking, we work from a Lagrangian point of view. Using the 2D cell tracking algorithm of Lochbihler, Lenderink, and Siebesma (2017), we can find continuous cells and track them in time. Continuous cells are formed from adjacent grid cells that meet our blocking index, i.e. when they have a value greater than zero. Another option for thresholds is the minimum area of a cluster in grid points. However, we want to limit blocks based on their area in km^2 rather than in grid cells, because the curvature of the earth leads to smaller surfaces for the same number of grid cells at higher latitudes compared to lower latitudes. Therefore we leave the minimum area at zero and filter out the smaller blocks afterwards, as will be described in Section 2.4.2.

Each continuous cell is assigned a unique ID in order to distinguish between different cells. For each of these continuous cells, the overlap with other continuous cells is checked for one time step backward and one time step forward. Two cells belong to the same track if there is some sort of overlap. Next to the straightforward initiation and termination of a track existing of one continuous cell moving in time and disappearing again, there are also other options. Multiple continuous cells can merge into one, and one cell can split up into multiple continuous cells. Each track is given its own unique ID and a number for its track type, making it possible to know how a track initiated or terminated. In practice, most blocks follow a single track or split up later in their lifetime, but it is not common for them to merge.

Because blocks can cross the anti-meridian, it is necessary to use periodic boundary conditions. This makes it possible for the tracker to recognise when a block crosses the anti-meridian and does not see it as a new block appearing on the other side. Whenever a block gets into contact with a certain boundary, it is also mentioned along with the track ID and the initiation and termination process.

2.4.2 Tracking output

The tracking output results in a lot of new information. Outputs that we get are the size, duration, intensity (both mean and maximum), shape, weighted center, onset date, track-type, and weather or not a block touched a boundary. From all this information, we start by selecting blockings with a minimal duration of four days. Then, we convert the size of the blocks, which is given in a number of grid cells, to km^2 in order to remove blocking smaller than 500.000 km^2. The shape of the block is not taken into account here, just their weighted centre. Converting the size is done by taking the intensity-based weighted average of the latitude of the block and using

$$dx \approx 2\pi R \cos\phi \frac{2.5°}{360°}, \tag{2.9}$$

where R is the radius of the Earth and 2.5° is the size of our grid cells. After both the small and short-lived blocks are removed, the propagation velocity of the remaining blocks is calculated. As the primary moving direction of blocks if zonally, we only take the zonal propagation velocity into account. This velocity is calculated by comparing the intensity-weighted center of a block at its onset date to its offset date and dividing this distance by the blocking duration. From this value, we can deduce if a block has an eastward of westward propagation component. Of course, the weighted centre of a block can also move within the outer boundaries of the block, or change its direction halfway during its lifetime, leading to uncertainties in the

outcome. However, we choose to keep working with it as it is the most straightforward way to calculate the zonal propagation velocity and is consistent with Steinfeld et al. (2018).

3 Results

3.1 Evaluation of the performance of ECE3p5 compared to ERA5

In this part of the thesis the results will be discussed, starting with the evaluation of the performance of ECE3p5 compared to ERA5. The ability of ECE3p5 to simulate atmospheric blocking will be tested for its frequency, its blocking intensity, its inter-model variability, and other blocking characteristics such as the number of blocks, size, duration, and the propagation velocity.

3.1.1 Blocking Frequency

The first blocking characteristic that will be evaluated is the blocking frequency. This blocking frequency is defined as the percentage of days a grid cell is blocked per year or season, for which the Lagrangian framework is not yet necessary as a gridcell is either blocked (index=1) or not blocked (index=0). In Figure 9, the frequency is shown for ERA5 (above) and for the difference between ERA5 and ECE3p5 (below) over the period of 1951-2014. Both for ERA5 and for the difference with ECE3p5, the frequency is plotted for the annual mean (first column), the winter mean (second column), and the summer mean (third column). In the lower subfigures, the contours show the percentage of blocked days for ECE3p5, while the shading indicates the differences in blocked days compared to ERA5. This figure is based on Figure 1 from Davini and d'Andrea (2020), where the same analysis is done for CMIP3, CMIP5, and CMIP6.

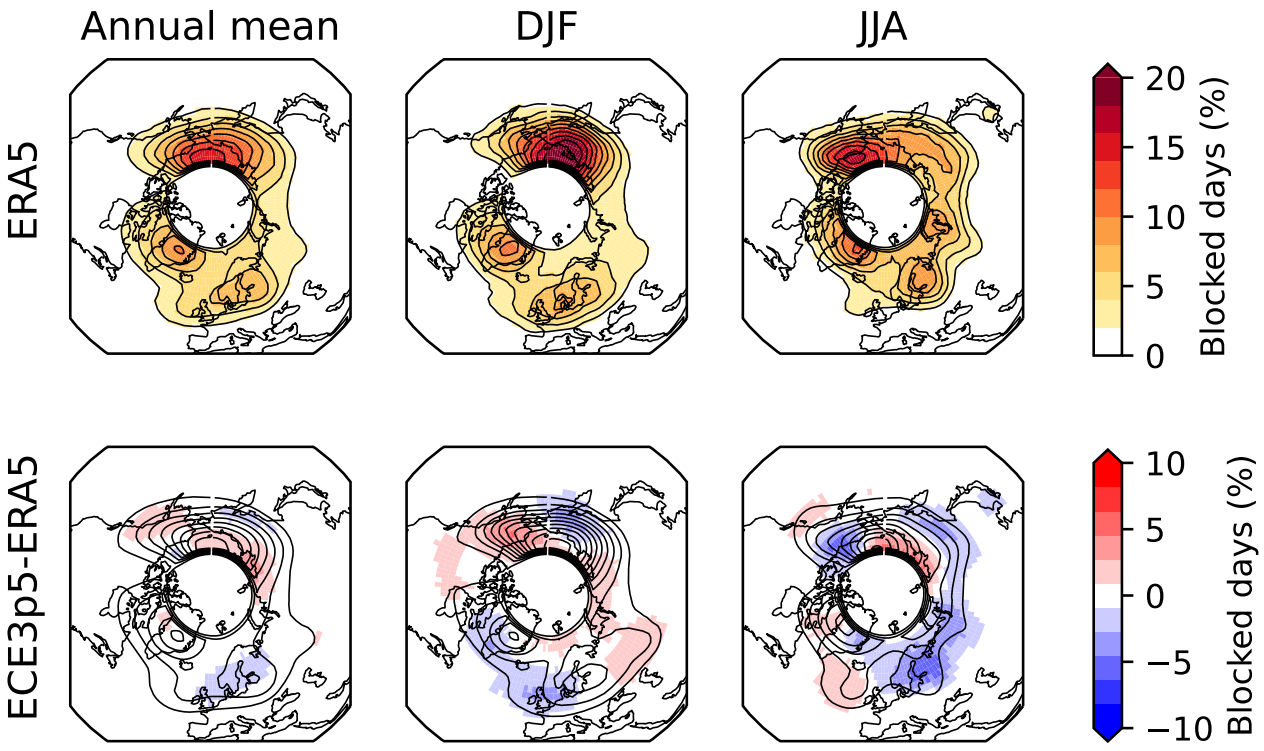

Figure 9: Upper row: Climatological blocking frequency ERA5 (contours and shading) for the annual mean, winter mean (DJF), and summer mean (JJA). Lower row: contours show blocking frequency of ECE3p5, shading shows the difference between ERA5 and ECE3p5 for the annual mean, winter mean, and summer mean. Both the data from ERA5 and ECE3p5 are taken over the period of 1951-2014.

Starting with the upper-left figure in Figure 9, in which the annual mean is taken of the ERA5 blocking climatology, we can see that atmospheric blocking is most frequent over the North Pacific, Greenland, and Scandinavia. The highest frequencies are found in the North Pacific, with values of up to 16% of blocked days per year. If we compare these ERA5 frequencies with those of ECE3p5, shown as contours in the lower-left

subfigure, we can see that our model follows the same patterns, but underestimates the blocking frequency over Europe by up to 1.6%, and overestimates the frequency over Alaska, the Bering Sea, and Siberia by up to 3.4%. Although these absolute differences lead to small percentages, the 1.6% underestimation makes up 25% of the original ERA5 frequency of 6.5%. For the overestimation over the North Pacific region, the maximum overestimation makes up 52% of the original 6.5%.

The second column shows the winter period, covering the months of December, January, and February (DJF). Comparing the ERA5 winter mean frequency with the annual frequency shows that blocking occurs more often in winter, although the blocking hotspots remain approximately the same. Blocking over Europe has shifted more towards Western Europe, and blocking over the North Pacific has shifted from the Bering Sea towards Siberia. The highest frequencies are again found over the North Pacific, where up to 20% of winter days are blocked. The differences with the ECE3p5 model are also bigger in winter. Underestimation is now found over Greenland, Western Europe and East Siberia with up to 3.5% (relative difference: 32%), while overestimation can be found over Alaska, Russia and Siberia up to 4.7% (relative difference: 54%). It is also noteworthy that over Europe, there is an underestimation over the Atlantic while there is overestimation over Russia, which could indicate an eastward shift of blockings. The same effect is seen over the North Pacific.

In the third column, the summer season frequency is shown over the months of June, July, and August (JJA). The ERA5 summer frequency has a different blocking pattern compared to the winter and annual mean: blocking is more confined to higher latitudes, and instead of three dominant blocking areas, blocking is more spread out over all longitudes. Compared to the annual mean, the frequency over Scandinavia is concentrated more over Finland, with an additional area of higher frequencies over the Ural. The blocking pattern over Greenland is about the same, although with slightly higher frequencies, while the blocking pattern over the North Pacific has concentrated over Alaska, with a tail over Siberia. The highest frequencies for ERA5 blocking in summer are found over Alaska with 17% of blocked summer days. Compared to the differences between ERA5 and ECE3p5 for the annual mean and the winter mean, the absolute differences in summer are relatively large. The map is dominated by large areas of underestimation over Scandinavia, Russia, and Alaska with values up to 6.3% (Relative difference: 64%). Smaller areas of overestimation are found over the Atlantic and North Siberia that stay within 5.3% (Relative difference: 48%). Overall, both the absolute and relative differences are greater in summer than in winter.

3.1.2 Blocking Intensity

For the blocking frequency, we only looked at the number of days a grid cell was blocked. However, this method does not take the different intensities of the blocks into account, as the index is either 0 or 1. When blocking intensity (BI) is added and annual, winter, and summer means are taken, we end up with the results shown in Figure 10. Adding the blocking intensity gives a better sense of where blocking is most prevalent. Starting again with the annual mean and comparing it with the frequency in Figure 9, the differences are mainly visible over the North Pacific. While the North Pacific dominates in frequency over Greenland and Scandinavia, this is no longer the case when the blocking intensity is added, resulting in a much more balanced distribution over the areas. More specifically, both the North Pacific and Scandinavia have a maximum mean BI of 0.22. This indicates that blocking over the Atlantic is stronger than blocking over the Pacific. The difference between our model and the reanalysis data shows the same pattern of anomalies for the BI as for the blocking frequency, with an underestimation over Europe and an overestimation over Alaska and Siberia, both within 0.06. In terms of relative differences, this comes down to an underestimation of 28% and an overestimation of 48%, which is comparable to the 25% and 52% of the under- and overestimation for the blocking frequency.

In winter, shown in the second column, we can see that the BI is generally higher than the annual mean, with values of up to 0.32. The main blocking areas for BI correspond to the pattern of the blocking frequency and also the differences between the model and ERA5 show largely the same pattern as before. Again, there are two regions with a dipole structure in the figure showing the model bias. Over the Atlantic and Greenland, we have an underestimation of 0.14 (Relative difference: 43%), while we have an overestimation over the Ural region of 0.08 (Relative difference: 67%), which had an intensity of 0.12 in ERA5. The other dipole is

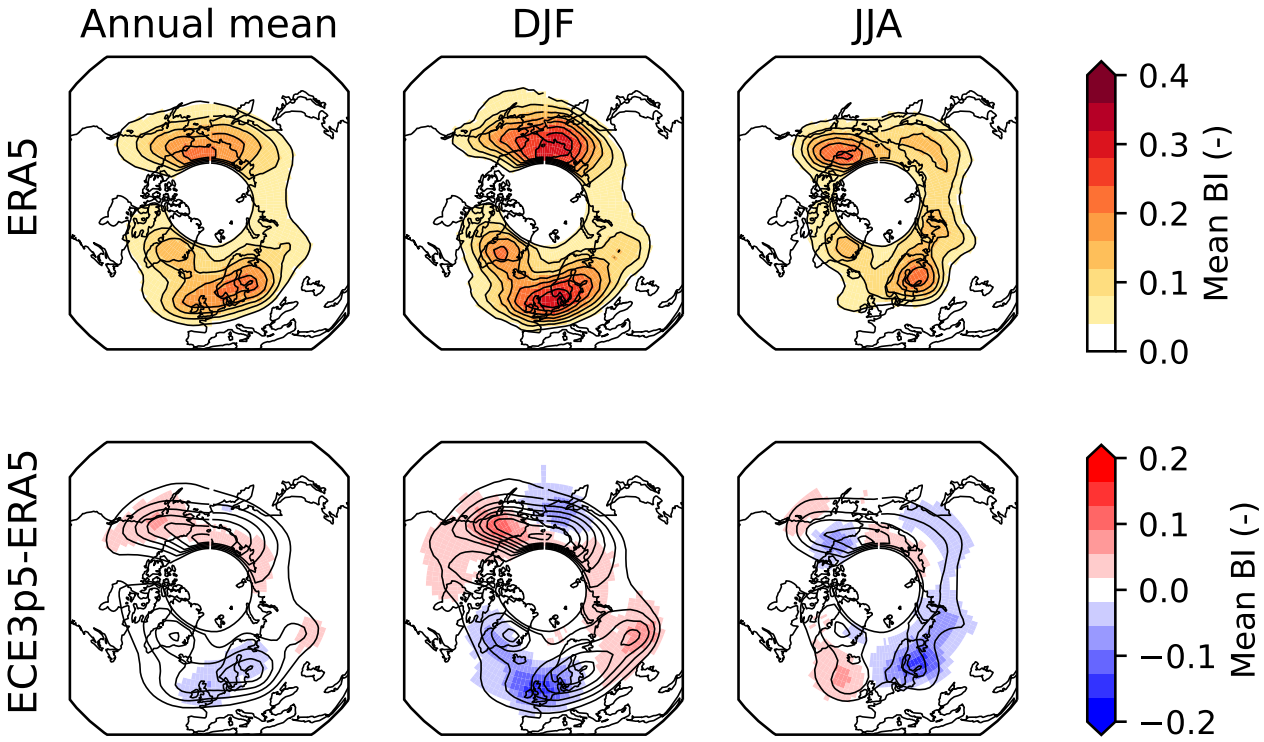

Figure 10: Upper row: Climatological blocking intensity ERA5 (contours and shading) for the annual mean, winter mean (DJF), and summer mean (JJA). Lower row: contours show blocking intensity of ECE3p5, shading shows the difference between ERA5 and ECE3p5 for the annual mean, winter mean, and summer mean. Both the data from ERA5 and ECE3p5 are taken over the period of 1951-2014.

situated over the North Pacific, where an underestimation can be found of 0.08 over the Bering Sea (Relative difference: 30%) and an overestimation over Alaska of 0.11 (Relative difference: 66%).

Lastly, we look at summer in the third column. Greenland is now less prominent than when we only looked at the frequencies, indicating that these blocks have a lower intensity in summer. Alaska and East Scandinavia are now the regions that dominate the picture with a BI of 0.25. In general, summer blocks seem to have a lower BI than in winter. The pattern for the differences between model and observations resemble the model bias for the frequency. A maximum overestimation is found over the Atlantic of 0.07. Compared to a mean BI of 0.04 for ERA5, which is even smaller than the overestimation, this leads to a relative difference of 175%. The largest underestimation is found over Finland with a difference of 0.14, which results in a relative difference of 63%.

3.1.3 Intramodel variance

The next aspect of our ECE3p5 model to be evaluated, is its intramodel variance, i.e. the variance between the ensemble members of the model. This intramodel variance, which is computed as the ensemble standard deviation, is a measure for the internal variability of the model and shows how well the different ensemble members agree with each other. In Figure 11, the intramodel variance between the 16 ensemble members is shown for the blocking frequency on the left, and for the blocking intensity on the right, both for winter (above) and summer (below). For the frequency in winter, the standard deviation between members stays within 0.6%, with the largest variability over Greenland and Alaska. In summer, the variance is slightly bigger with a standard deviation of 0.7%, mostly over Greenland and Siberia. Compared to the frequencies of blocking in ERA5, which were up to 20%, these values of 0.6% and 0.7% are really small, namely 3% and 3.5%. Even compared to the model bias with its values around $4-6\%$, the largest values of the intramodel variance make up about $35-10\%$ of this difference. The standard deviations in blocking intensity are larger

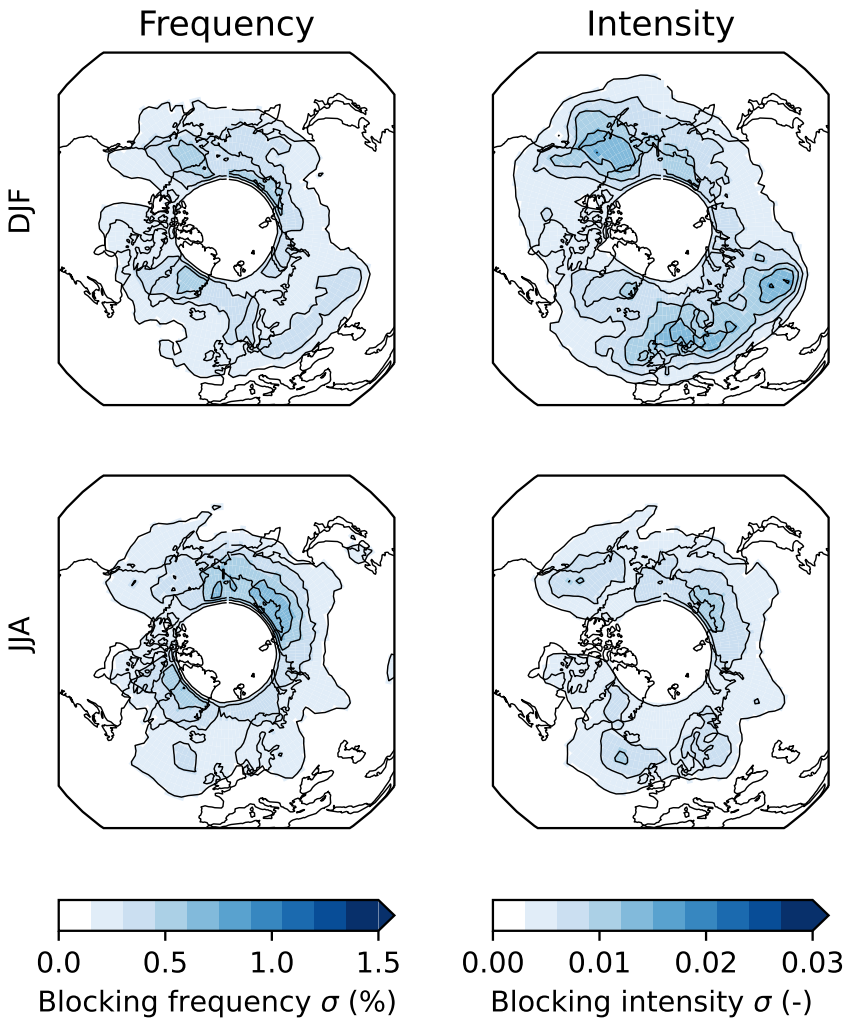

Figure 11: Standard deviation of climatological blocking frequency (left) and blocking intensity (right), for the winter season (DJF, above) and summer season (JJA, below). The standard deviation shows the variability between the 16 ensemble members of ECE3p5 over the whole historical dataset, running from 1850-2014.

for the winter season and smaller for the summer season. The largest values in winter are up to 0.02, which is 6.25% of the largest BI of 0.32. In summer, the largest values reach a standard deviation of 0.01, which is 4% of the largest BI in summer of 0.25. From these results we can see that the uncertainty in the blocking simulations is more probable to result from the model properties then from the internal variability of the model.

3.1.4 Lagrangian blocking characteristics

Blocking frequency and blocking intensity are both blocking characteristics that can be evaluated without using a Lagrangian framework. However, this Lagrangian framework, which we achieve by using the 2D celltrack algorithm explained in Section 2.4, is necessary if we want to know more about individual blocks and their characteristics. The output of the celltrack algorithm provides us with information on the number of blocks per year, the size of the blocks during their lifetime, their duration, the average blocking intensity, the maximum blocking intensity, and finally their zonal propagation velocity. All this information is summarised in Table 1 for ERA5 and ECE3p5 for their annual and seasonal (winter/summer) values. The standard deviations are taken over all 16 ensembles and all blocks within these ensembles.

	# Blocks (yr^{-1})	Size ($\cdot 10^6$ km^2)	Duration (d)	BI_{av} (-)	BI_{max} (-)	Velocity (km d^{-1})
ERA5						
Annual mean	117 ± 9	1.1 ± 1.0	5.8 ± 2.3	1.8 ± 1.0	2.4 ± 1.2	134 ± 347
Winter	24 ± 4	1.5 ± 1.3	5.8 ± 2.2	2.2 ± 1.2	3.0 ± 1.5	117 ± 386
Summer	36 ± 4	1.0 ± 0.8	6.0 ± 2.5	1.4 ± 0.7	1.8 ± 0.8	97 ± 322
ECEp5						
Annual mean	107 ± 8	1.3 ± 1.1	5.8 ± 2.3	1.9 ± 1.0	2.5 ± 1.3	102 ± 382
Winter	25 ± 4	1.6 ± 1.3	5.7 ± 2.1	2.2 ± 1.2	3.1 ± 1.4	99 ± 439
Summer	28 ± 4	1.1 ± 0.9	6.0 ± 2.5	1.4 ± 0.7	1.9 ± 0.9	73 ± 326

Table 1: Blocking statistics over the period of 1951-2014 for ERA5 (above) and ECE3p5 (below). Significant differences between ERA5 and ECE3p5 are shown in red. Variability is given in one standard deviation over all blocks within the specified season.

The first blocking characteristic in the table is the number of blocks per year, taken over the whole year and per season. ECE3p5 underestimates the number of blocks over all time periods, although the winter values do not differ significantly according to the t-test. As the annual mean difference is about 10 blocks per year and summer is 8 blocks per year, summer seems to be the main contributor to this annual underestimation, indicating that the model has greater difficulty simulating the right amount of blocks in summer than in winter.

The number of blocks per year is the only variable where significant differences are found between the reanalysis data and the model. Especially duration, average blocking intensity and maximum blocking intensity are almost identical to each other, meaning that the model does a decent job in simulating these blocking characteristics. Combined with Figure 10, the differences in blocking intensity between the ERA5 reanalysis data and ECE3p5 are therefore most probably due to the differences in frequency and blocking location between the datasets, and not the simulation of the blocking intensity itself.

Continuing with the surface area of the block, the variability is almost as large as the mean surface itself, indicating the large differences between individual blocks. Both for the reanalysis data and the model, blocks have a bigger surface area in winter than in summer. The mean duration does not differ significantly over the seasons, as the summer blocks are on average only 0.2 and 0.3 days longer for respectively ERA5 and ECE3p5, which is small compared to their standard deviations. The values for the average and maximum velocity tell the same story as Figure 10, where we could see that winter blocks on average have a higher BI than the annual mean, while summer blocks have a lower BI. From the values in the table we can see that not only the absolute values of the BI are higher in winter and lower in summer, but so is their variability.

The last blocking characteristic is the zonal propagation velocity. The values for the propagation velocity differ between ERA5 and ECE3p5, but are not significantly different due to their large variability, which even exceeds the mean velocity values. Despite the general conception that blocks are quasi-stationary, we can see that the mean propagation velocity is eastward for both the reanalysis data and the model. This same eastward trend was also observed by Steinfeld et al. (2020) using PV anomalies. The variability also shows the existence of blockings moving in the westward direction, against the prevalent eastward current.

3.2 Characteristics of the propagation velocity of blocking in ECE3p5

After the evaluation of the performance of ECE3p5 compared to ERA5, we continue with the behaviour of atmospheric blocking in ECE3p5. In order to understand the characteristics of the propagation velocity of atmospheric blocking, we first look at its seasonality, followed up by an analysis of the propagation velocity in relation to other factors, and finally an assessment of the spatial distribution of different blocking propagation directions. As we expect eastward moving blockings and westward moving blockings to behave differently, we split them up and evaluate them separately.

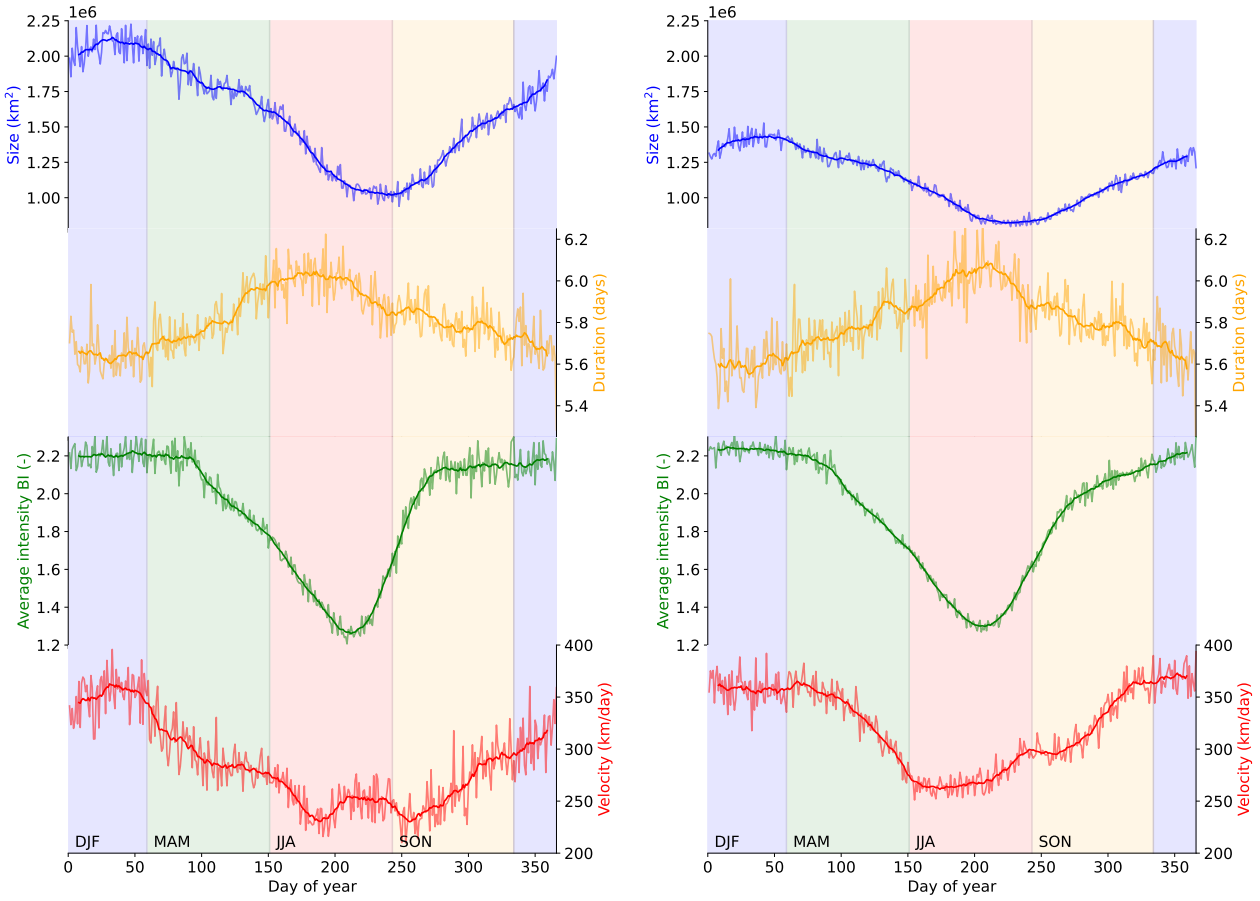

(a) Westward-moving blocks

(b) Eastward-moving blocks

Figure 12: Blocking characteristics for (a) westward and (b) eastward moving blocks. The characteristics shown are the mean size (blue), the duration (yellow), the average intensity (green), and the absolute propagation velocity (red) over the years of 1850-2014 and all 16 ensembles. The thicker lines are the 15 day rolling means, and the thinner lines show the mean values over all blocks and ensembles per day of the year.

3.2.1 Seasonality

To complement earlier research (see Section 1) on the analysis of duration, frequency, intensity, and extension, we now add the seasonality of the propagation velocity and compare it with the other variables. These different variables have been plotted in Figure 12 for their seasonality per day of the year. The thin lines show the daily mean values over all 16 ensembles and 164 years (1850-2014), and the thick line resembles the 15 day rolling mean. In Figure 12b, the eastward moving blocks are shown and in Figure 12a the westward moving blocks are shown.

The blocking propagation velocity (red in Figure 12) is the first variable to be examined and later compared with the other variables. It is plotted in absolute values for both the eastward-moving and westward-moving blockings to allow for better comparison. Both the eastward and the westward velocities have a seasonal cycle with higher values in winter, a decrease in the propagation velocity in spring, a minimum in summer, and an increase in velocity again in autumn. There are also some differences. On average, the eastward blockings have a higher propagation velocity than the westward-moving blocks over all seasons, although they approach each other when spring turns into summer and at the end of winter. They both have their maximum velocities in winter, with a value of 373 ± 39 km d^{-1} for the eastward blocks and 364 ± 42 km d^{-1}

for the westward blocks, where the variability is given as one standard deviation over all ensemble members and years on that specific day of the year. The eastward-moving blocks have their maximum at the end of December, while the westward-moving blocks have their maximum in the beginning of February. However, as the eastward moving blocks have roughly the same velocity throughout the whole winter, this maximum is more spread out than for the westward-moving blocks. Their minimum velocities are also different, as the eastward velocities have their lowest value in June (261 ± 39 km d^{-1}), while the westward velocities have their lowest values in July and September (230 ± 42 km d^{-1}). Over the year, both blocking directions thus exhibit roughly the same seasonality, but with shifts in their minima and maxima of one to two months and larger values for eastward-moving blocks.

After the division of all atmospheric blocks over westward-moving and eastward-moving blocks, the other blocking characteristics are also split up according to their zonal direction, leading to the different sizes (blue), durations (yellow), and intensities (green) for the eastward-moving blocks in Figure 12b and the westward moving blocks in Figure 12a. When we split up the size of the blockings with respect to their propagation direction, a clear distinction arises between the size of the blocks that move to the west and that move to the east. Over the seasons, westward-moving blockings are constantly larger than eastward-moving blockings, although those differences are bigger in winter than in summer. Both have their maximum size at the end of winter, with values of $1.4 \pm 0.2 \cdot 10^6$ km^2 for the eastward variant and $2.1 \pm 0.4 \cdot 10^6$ km^2 for the westward variant. Their minimum size is found at the end of summer, with values of $0.8 \pm 0.2 \cdot 10^6$ km^2 for the east and $1.0 \pm 0.4 \cdot 10^6$ km^2 for the west. Apart from the differences in size, there are no clear differences in the seasonality between the two blocking directions. This leads to an interesting misalignment of two months between the minimum velocity and the minimum size for eastward propagating blocks, while the minimum value of the size of the westward propagating blocks can be found in the middle of its velocity minima.

The next variable is the duration of the blocks. Just as we saw in Table 1, the differences over the seasons are small. The same thing can be said of the different blocking directions, which only have minor differences compared to each other. Both the eastward and westward blocks have the same values for their minima and maxima, with a minimum value of 5.6 ± 0.2 days and a maximum value of 6.1 ± 0.2 days. This results in a difference of 0.5 ± 0.2 days between the minima and maxima of the blocks. Within these small differences, the blocks have their maximum for both cases in July and their minima both in winter. Compared to the propagation velocity, blocks have the shortest duration in the same season when they have their highest velocity, and their longest duration when they have the lowest velocities in summer.

The final variable is the average blocking intensity. As with duration, there is a clear seasonality to blocking intensity, which is roughly the same for blocks moving in both directions. Both have a constant average intensity over the winter and parts of spring and autumn, and then decline in summer. The only difference seems to be that the transitions between the steady state in winter and the minimum value in summer is more abrupt for the westward-moving blocks compared to the eastward-moving blocks. Both have minimum values of 1.3 ± 0.3 in July and maximum values of respectively 2.3 ± 0.3 and 2.2 ± 0.3 in winter for eastward and westward blocks. Over the year, the average intensity is higher in during seasons where blocks also have a higher propagation velocity, and lower in seasons with lower propagation velocities.

Another way to illustrate all these characteristics and their seasonal relations is shown in Figure 13, where the climatological values for size and velocity are plotted against each other, with intensity as the scatter size. Duration is left out of this figure, as its differences over the seasons are small. No new information can be found in this figure compared to Figure 12, but it nicely illustrates the differences in behaviour between the two blocking directions. The westward-moving blocks are more seasonally aligned in size and velocity than the eastward-moving blocks, which have a large sudden drop in size in summer. This drop was illustrated as the phase differences in Figure 12b. The larger spread in winter in both size and velocity is also visible for the westward-moving blocks compared to the eastward-moving blocks, where all blue dots are much closer to each other. The second minimum value in autumn for westward-moving blocks is also visible in the small return towards lower velocities.

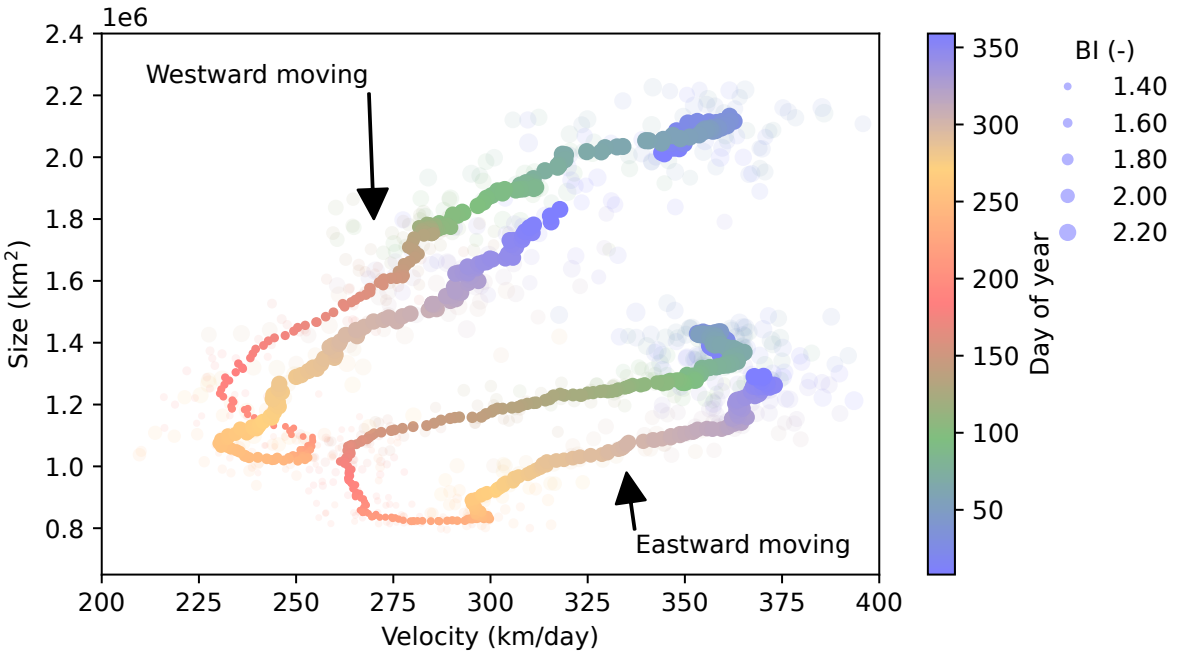

Figure 13: Climatological values per day of the year for size (km^2) against absolute values of the propagation velocity (km/day). The scatter size indicates the blocking intensity (-), and the colour the day of the year. Each day of the year is averaged over the period of 1850-2015 over all 16 ensemble members (light colours), and a 15-day running mean is plotted (opaque colours).

3.2.2 Relation between propagation velocity and other characteristics

After the seasonality, we look at all winter and summer blocks separately, which allows us to study any correlations between the different blocking characteristics and the propagation velocity. In Figure 14, the propagation velocity is plotted against the size of the block, the duration, and the average intensity, all for winter and summer. As we are dealing with large amounts of data, in total 64603 winter blocks and 74270 summer blocks, a kernel density estimation (KDE) is used to generate the probability density functions. In addition, the 10^{th}, 50^{th} and 90^{th} percentiles are used to mimic the behaviour of the two extreme states and the mean state of the size, duration and intensity per velocity bin of 40 km/day. For the faster velocities, the number of blocks within these velocity bands decreases. This results in more noise in the percentiles for the size, duration, and intensity towards the faster velocities, making the results less robust at the more extreme velocities.

In Figure 14, the size is shown in the first column, with the winter months at the top and the summer months at the bottom. From the KDE, it is noticeable that the blocking size is much more confined to smaller sizes in summer, while the spread is larger in winter. The majority of the blocks in both winter and summer are on the smaller side compared to the total spread and are associated with eastward velocities. The largest blocking sizes are however associated with westward velocities. This uneven allocation becomes even more clear when looking at the percentiles, which represent the 10% smallest, the 10% largest blocking sizes, and the mean size per velocity bin. For both seasons it is visible that the larger the block, the faster the block moves westward. Towards the quasi-stationary blocks, the blocking size decreases. In winter, the blocking size then stays approximately the same when moving towards eastward propagation velocities, while in summer the blocking size slightly increases again. This result can be related to Rossby wave theory, which was explained in Section 1 and Equation 1.2, where the group velocity c_g in Equation 1.2 is westward for larger waves and eastward for smaller waves. The similarity in behaviour between blocking and Rossby waves stresses the link between the two phenomena.

In the second column of Figure 14, the duration of the blocks is plotted against their propagation velocity.

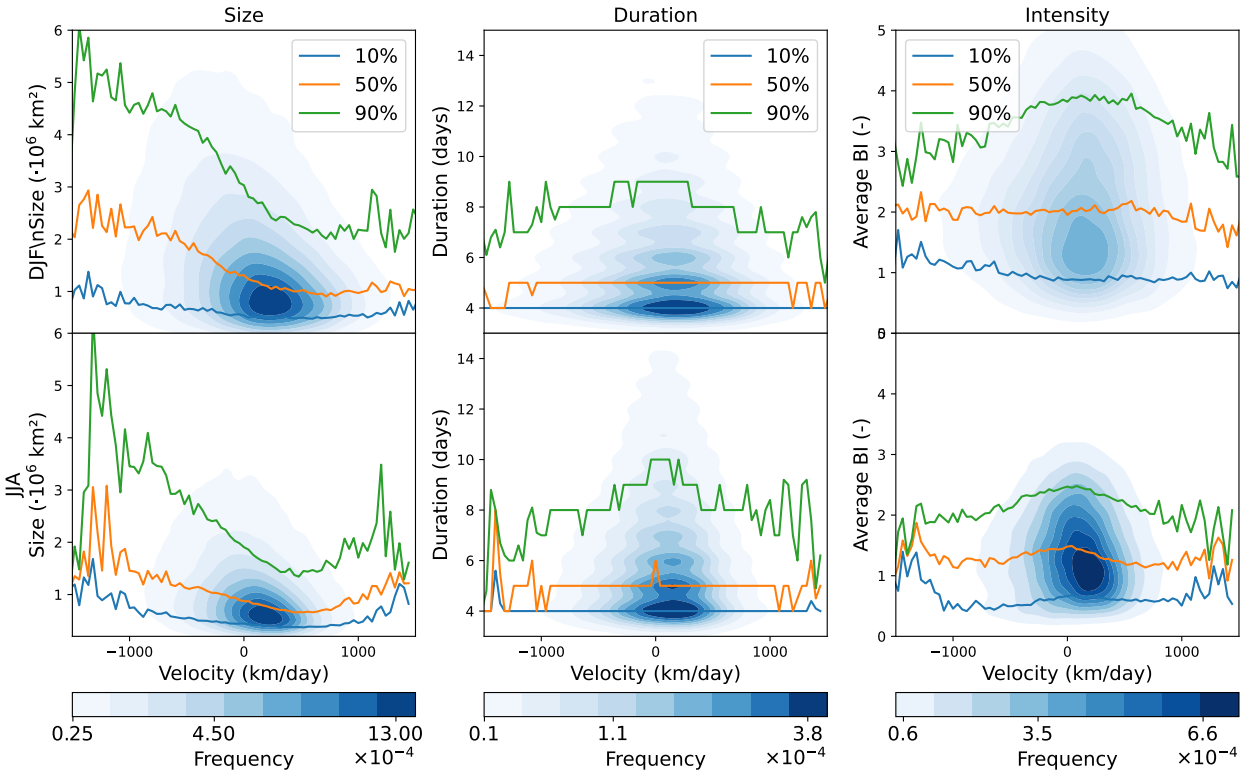

Figure 14: Kernel density estimation (blue shading) and the 10^{th} (blue), 50^{th} (orange) and 90^{th} (green) percentiles for the size (first column), duration (second column), and intensity (third column), all for winter (DJF, above) and summer (JJA, below). Taken over the period of 1850-2014 over all 16 ensembles of ECE3p5.

The KDE for the duration is not as smooth as for the size or intensity. This is due to the discrete way in which the duration is measured, which is in whole days, whereas the size and intensity are measured in continuous values. The KDE is pyramidal for both winter and summer, with the longest durations over the stationary blocks. In both seasons, it can be seen that blockings with shorter duration occur more frequently than blockings with longer duration. Because of the discrete values of the duration, the percentiles are also more choppy. The 90^{th} percentile shows for both winter and summer that stationary blocks have a longer duration than the faster propagating blocks. The 50^{th} percentile, which shows the mean value per bin, is 5 days for almost all velocities and therefore does not show the same relationship as the 90^{th} percentile line. The 10^{th} percentile is a straight line at four days, which is the minimum duration threshold that we set in Section 2.

The final blocking characteristic that is compared to the propagation velocity, is the average blocking intensity in the third column. The first notable difference between winter and summer is the spread in the data, as shown by the KDE. The winter months exhibit a much larger variability and higher values than the summer months. Both seasons display an oval distribution around slightly eastward moving velocities, with a denser core for lower intensities. This indicates that the more stationary blocks display the largest range in blocking intensities. For the percentiles in winter, only the 90^{th} percentile shows this same relationship of larger intensities for quasi-stationary blocks. The 50^{th} and 10^{th} percentiles do not show this, and stay around the same BI no matter the propagation velocity, which can also be read from the broader base of the KDE. In summer, the 90^{th} and 50^{th} percentiles show a larger BI for quasi-stationary blocks and lower strengths for faster moving blocks, although they also have a lot of noise for the fastest moving blocks. The sign in the 10^{th} percentile is minimal.

Combining all the information in Figure 14 roughly tells us that quasi-stationary blocks are smaller, have a longer duration, and are stronger, while faster moving blocks are larger, last shorter, and are weaker. It is

interesting to see which of these factors will be most important in determining the effect these blocks have on temperatures at the surface. This will be studied in Section 3.3. Before moving on to this blocking impact on temperatures, we first examine where blocks with different propagation velocities reside.

3.2.3 Spatial distribution of different blocking velocities

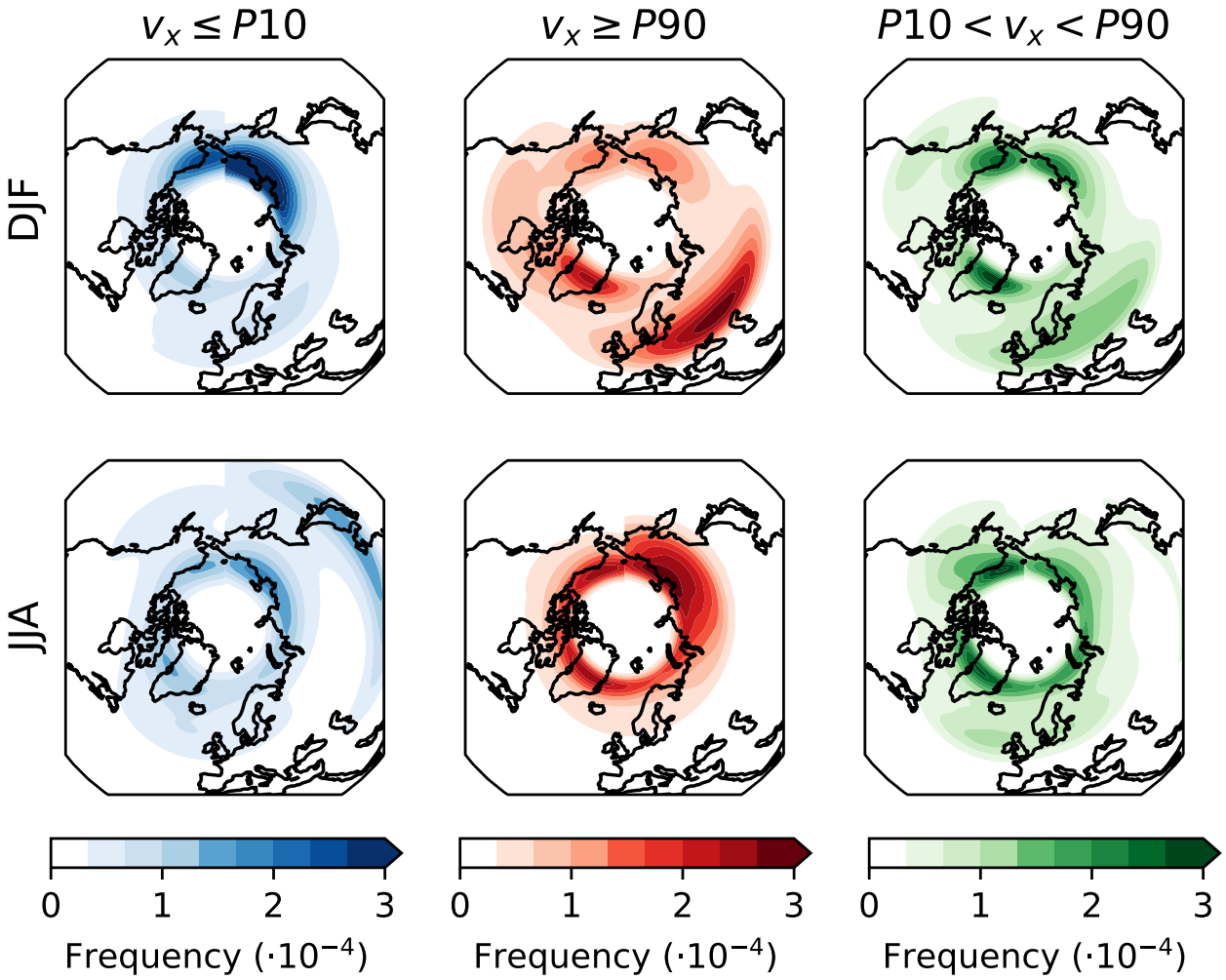

Figure 15: Spatial distribution weighted blocking centres with respect to the blocking intensity, on the fourth day, of the 10% fastest westward-moving blocks ($v_x \leq P10$, first column, total DJF/JJA: 8479/6451 blocks), the 10% fastest eastward-moving blocks ($v_x \geq P90$, second column, total DJF/JJA: 8582/3965 blocks), and all propagation velocities in between ($P10 < v_x < P90$, third column, total DJF/JJA: 47542/63854 blocks), taken separately over all winter months (DJF, above) and over all summer months (JJA, below) over the period of $1850 - 2014$ for all 16 ensembles of ECE3p5.

Due to the different behaviour of eastward-moving blockings and westward-moving blockings in terms of seasonality and in relation to other blocking characteristics, it is of interest to investigate whether there are also differences in their spatial distribution. For this purpose, the blocks were categorised into three groups: the 10% fastest eastward moving blocks ($v_x \geq P90$), the 10% fastest westward moving blocks ($v_x \leq P10$), and all blocks in between ($P10 < v_x < P90$). For each blocking type, we determined the coordinates of the weighted centres of the blocks based on their BI on the fourth day of their existence. The choice of the fourth day aligns with the division made by Steinfeld et al. (2018) between onset days and mature days of the block, with the mature phase considered to be between day three and day five. By focusing on the

fourth day, we ensure that we assess the blocks during their mature phase. This analysis was performed for both for winter and summer, resulting in Figure 15. It is important to note that the 10% fastest eastward- and westward-moving blocks do not have the same velocities in winter and summer, as is evident from the distinct distributions in Figure 14. The 10% fastest westward-moving blocks have a velocity faster than 462 km/day in winter and 345 km/day in summer, while the 10% fastest eastward-moving blocks have a velocity faster than 623 km/day in winter and 458 km/day in summer. Additionally, it should also be kept in mind that the distribution shown in Figure 15 is only a representation of the centers of the block and not their entire spatial extent. Lastly, it is important to see the following results in the light of Figure 9, where it was shown that in certain regions the blocking frequency was over- or underestimated by the model. These over- and underestimations also work trough in the frequencies shown in Figure 15.

The spatial distribution differs per type of block. In winter, the fastest 10% of eastward-moving blocks are predominantly located over Eastern Europe, extending into the Ural region of Russia, and exhibit a secondary concentration over Greenland. The region over Europe and Russia is particularly striking, as this region is not so prominent in the third column, where the majority of blocks are represented. The hotspot over Greenland is also visible for the majority of the blocks in the third column, indicating that it is not limited to the fastest eastward-moving blocks. The second column illustrates that the fastest 10% of westward-moving blocks are primarily situated over Siberia, extending to the northern areas of Alaska. This region is not as prominently blocked in the third column, highlighting it as a specific area for westward-moving blocks.

The spatial distribution of summer blocks differs from that of winter. As observed in Figure 9, summer blocks are mostly confined to the higher latitudes. For the 10% fastest eastward-moving blocks, the blocking centres are found in a narrow band over the higher latitudes, with a higher concentration over Siberia. This pattern resembles the distribution observed for the 10% fastest westward-moving blocks in winter. In summer, these fastest westward-moving blocks do not exhibit a specific dominant area; instead, they are more evenly distributed over the higher latitudes. Notably, a small band over the lower latitudes around Japan stands out, as it is absent in the third column for the majority of the blocks. For the majority of the blocks, the highest concentrations are observed over Greenland and Northern Siberia.

3.3 Influence of the propagation velocity on temperature in ECE3p5

In Section 3.2.2, we examined the relationship between various blocking characteristics and propagation velocity. Figure 14 revealed that quasi-stationary blocks tend to have longer durations and higher intensities, making them more likely to have a significant impact on our weather. For the blocking size on the contrary, the fastest westward-moving blocks exhibited larger surface areas, while quasi-stationary blocks were generally smaller in size. Considering that both larger and more stationary blocks are expected to contribute to higher temperature anomalies, it is important to determine which factor holds a higher influence. First, we compare temperature anomalies with different propagation velocities of blocks in Section 3.3.1. Subsequently, we assess the impact of blocking size compared to velocity on temperature anomalies in Section 3.3.2.

3.3.1 Relation between temperature anomaly and the propagation velocity

To investigate whether the propagation velocity has an effect on the temperature anomalies resulting from the block, we divide the $40° \times 80°$ area around the block into four quadrants: the upper-left, upper-right, lower-left, and lower-right quadrants. From these quadrants, the average temperature anomalies are taken. It is necessary to distinguish between these areas because the temperature anomalies upstream and downstream of a block can differ in sign. Averaging over the whole area creates the possibility of lower mean temperature anomalies as the positive and negative values cancel out. We also distinguish between temperature anomalies measured over both land and sea, and those measured over land only. The results for the lower-right quadrant are evaluated here for both land and ocean in Figure 16, and for land only in Figure 17. The other quadrants can be found in Appendix C. As the quadrants mostly differ in their temperature anomalies but not so much in the patterns related to the propagation velocities, we choose to discuss just one of them here.

The temperature anomalies over both land and sea are plotted against the propagation velocities in Figure 16 for winter and summer. in the KDE plot in winter, a broad range of temperature anomalies is observed,

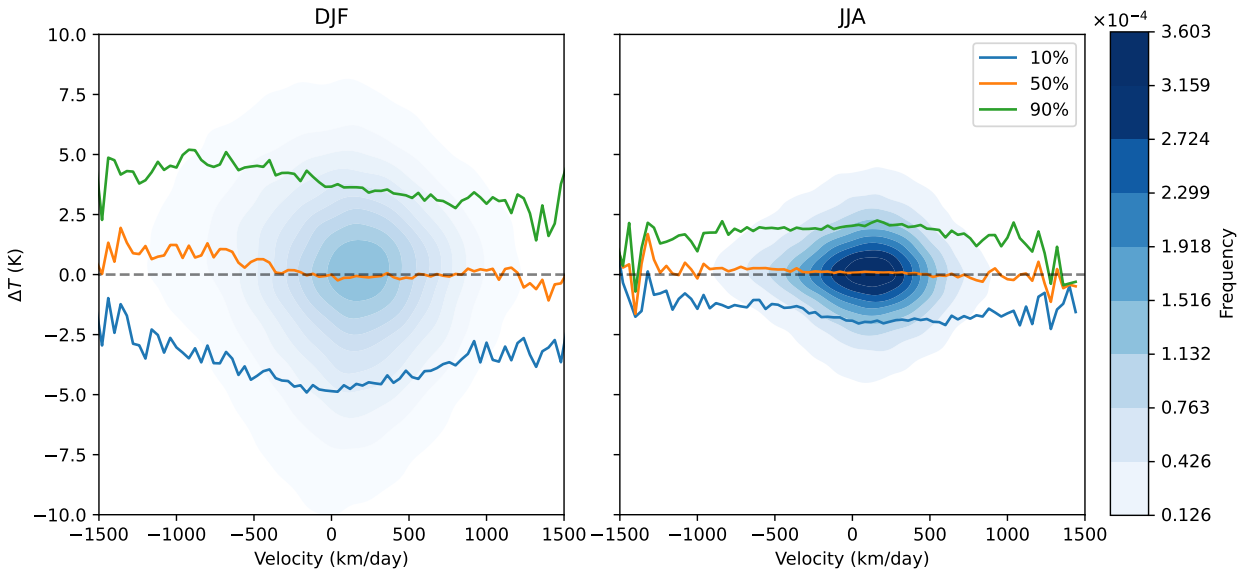

Figure 16: Kernel density estimation (blue shading) and the 10th (blue), 50th (orange) and 90th (green) percentiles of the 2m temperature anomaly plotted against the propagation velocity, all for winter (DJF, left) and summer (JJA, right). All blocks are taken into account, both over land and ocean. Taken over the period of 1850-2014 over all 16 ensembles of ECE3p5.

ranging from −10°C to 7.5°C. The majority of blocks result in relatively small temperature anomalies, as is indicated by both the KDE plot and the 50^{th} percentile, which fluctuates around zero degrees for the most part. This is in line with our earlier results in Figure 14, where it was shown that the majority of the blocks are relatively small, of short duration, and relatively weak. These blocks result in lower temperature anomalies, moderating the mean values. However, for westward velocities exceeding 500 km/day, the temperature anomalies shift towards positive values. The 10% warmest and coldest temperature anomalies both vary between approximately 2.5°C and 5°C. The 10% coldest temperatures predominantly occur in the presence of stationary blocks, indicating a correlation between lower temperatures and stationary blocking conditions. This result is in line with the research done by Brunner, Hegerl, and Steiner (2017), who showed that cold spells take longer to develop due to the slow process of horizontal advection of cold air. Conversely, the 10% warmest temperatures seem to exhibit a slight tendency to occur in conjunction with westward moving blocks. Although winter blocks are mostly related to cold spells (as discussed in Section 1), this figure clearly demonstrates that these winter blocks can generate a wide range of temperature anomalies, not limited to negative values.

In contrast to the winter conditions, the temperature anomaly differences in summer exhibit a more constrained distribution. The KDE plot displays smaller excesses, the 50^{th} percentile remains about zero, and the 10% warmest and coldest temperature anomalies do not exceed 2.5°C. Notably, none of the percentiles exhibit a discernible trend, as their values remain relatively consistent across the entire range of propagation velocities. The insensitivity of the temperature anomalies with respect to the propagation velocities can be attributed to the different warming process in summer, which is caused by both diabatic and adiabatic warming (again as discussed in Section 1). These processes occur more rapidly than air advection, and Figure 16 demonstrates that the warming effect can still take place beneath faster-moving blocks. Especially for Rex blocks, this warming underneath the block goes hand in hand with cooling underneath the accompanying lower pressure area to the south of the block. These lower temperatures are represented by the 10% lowest temperature anomalies in Figure 16. The relatively small temperature anomalies observed in summer compared to winter can be attributed to multiple factors. Firstly, the data used for this analysis consists of daily mean temperatures. The cloud-free conditions that cause warming underneath the block during the day, also cause the cooling during the night. These lower night temperatures moderate the overall daily mean values. To quantify this effect, it would be necessary to study the differences in response between the minimum and

maximum temperatures. Secondly, as argued by Cheung, Zhou, Mok, et al. (2013), the continent is already warmer in summer, leading to lower temperature anomalies. Additionally, pressure gradients are smaller compared to winter. This last argument can be compared to the blocking intensity that we studied in Figure 12, where indeed summer blocks generally exhibit lower blocking intensities compared to winter blocks.

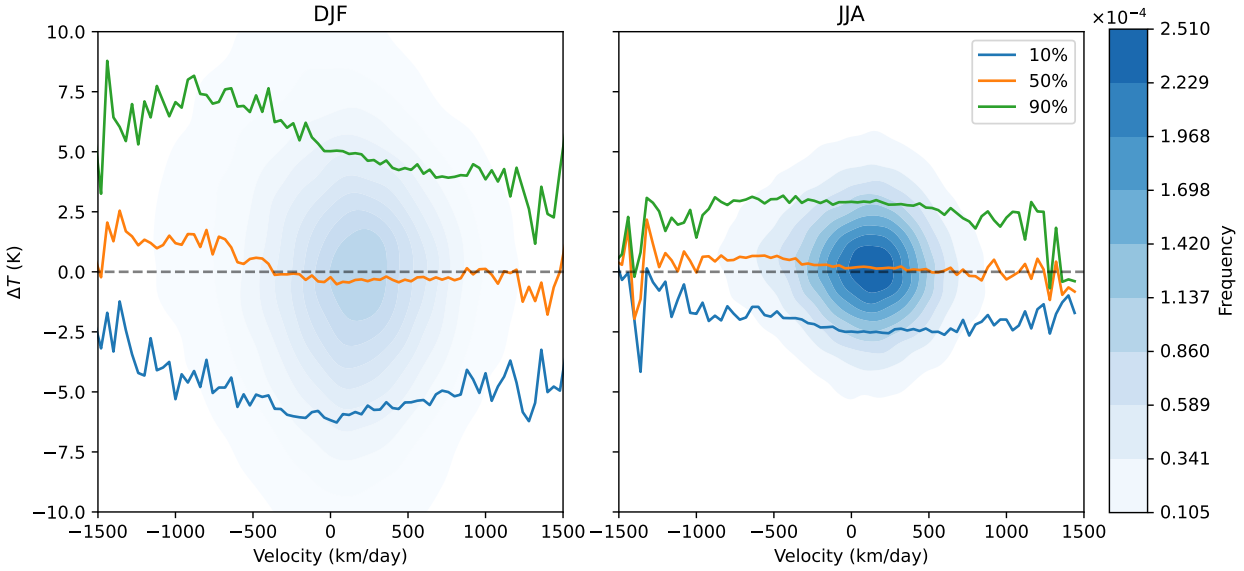

Figure 17: As in Figure 16, but for the 2m temperature anomalies over land only.

For Figure 16, the analysis encompasses both blocks that occur over land and those that occur over the ocean. However, the ocean has a significantly larger thermal warming capacity compared to land. Consequently, it takes longer for the surface area underneath the block to warm or cool over the ocean. At the same time, the temperature effects of blocking are primarily experienced on land, where the human population resides. Therefore, it is the land surface temperature anomalies that are of particular relevance when considering the impacts of blocking events. These land surface temperature anomalies are depicted in Figure 17. Notably, these anomalies are more pronounced for both winter and summer seasons. While in summer any relation between the propagation velocity and the temperature anomalies remains absent, we can see a stronger correlation between the two variables in winter. The coldest temperatures are still associated with low propagation velocities, just as was concluded from Figure 16. The relation between the warmest temperature anomalies and the propagation velocity however, is now much more pronounced. The warmest temperature anomalies can be associated with the faster westward-moving blocks, which creates an interesting contrast between the blocking velocities associated with the coldest temperatures. The pattern of the warmest 10% looks similar to the plot of the size versus the propagation velocity in Figure 12, so possibly the larger block size associated with faster westward-moving blocks plays a role in these larger temperature anomalies.

3.3.2 Dependence of the temperature anomaly on blocking size and propagation velocity

In order to assess the different effects of propagation velocity and size on temperature anomalies, a composite analysis is performed in which all blocks are divided according to their size and propagation velocity. This result is shown for blocks over both land and ocean in Figure 18, and over land only in Figure 19. On the x-axis, the percentages show the size per 20%, from small (0%) to large (100%). On the y-axis, the propagation velocities are sorted from the largest negative values (0%), to the largest positive values (100%). For both figures and both the winter and summer season, the quasi-stationary blocks with a velocity closest to zero are found at roughly 40%. The choice to use percentiles and not absolute differences in size or propagation velocity was made to ensure that every composite mean has enough cases for a reliable result. As a consequence, the percentiles do not represent the same velocity or size values for winter and summer, as

the percentages are taken separately for the two seasons. The percentiles do represent the same values per respective season in Figure 18 and Figure 19, as the only difference here is the temperature field taken into account. The values that the percentages represent are shown in Table 2.

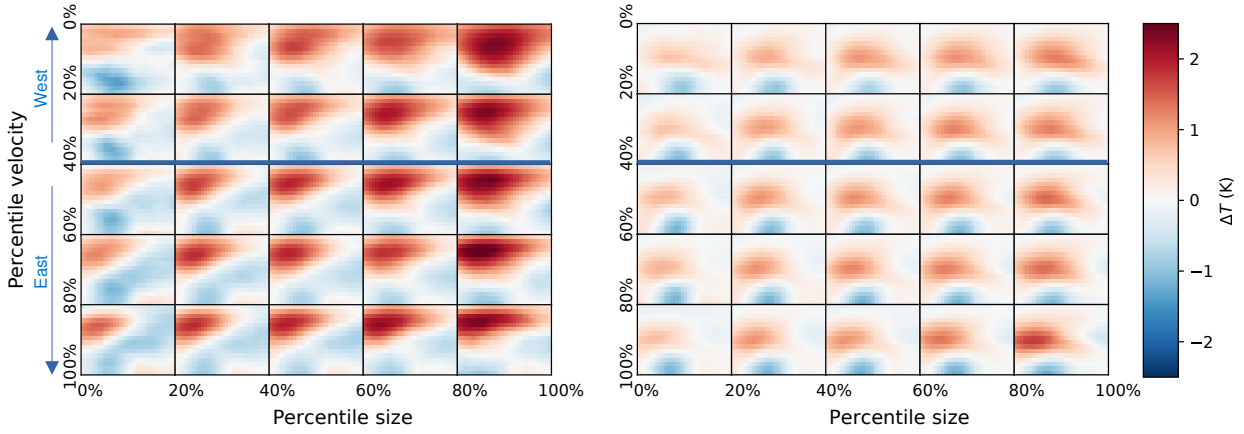

(a) DJF (b) JJA

Figure 18: Composite mean of 2m temperature anomalies in a region of $40° \times 80°$ around the blocking centre over both land and ocean. The winter season (DJF) is shown in (a), and the summer season (JJA) in (b). On the x-axis, the size is divided by its percentiles, going from small to large. On the y-axis, the propagation velocity is divided by its percentiles, going from negative values to positive values. The blue line indicates the division between westward-moving blocks and eastward-moving blocks, also indicated by the arrows. Data is taken from ECE3p5 over the period of 1850-2015 and over all 16 ensembles.

Figure 18 shows the composite mean analysis for winter (a) and summer (b) over both land and ocean. Focusing on winter, it is evident that for every combination of size and propagation velocity, a distinct pattern emerges. Positive temperature anomalies are consistently observed to the northwest of the block, while negative temperature anomalies are consistently observed to the southeast of the block. For all of them, the positive temperature anomalies dominate in value over the negative temperature anomalies. When we compare blocks with different sizes for the same propagation velocity, the temperature anomalies become stronger and take over a larger part of the selected area around the block. This result is to be expected, as a larger block will influence the temperature over a larger area. Comparing blocks with different propagation velocities but with the same size reveals a change in the temperature pattern. In the case of westward-moving blocks, the surface area surrounding the block exhibits a larger proportion of positive temperature anomalies, primarily concentrated to the north of the block, extending towards the blocking centre. The faster eastward a block moves, the more confined the positive temperature anomalies are to the northwest, leaving more room for the negative temperature anomalies.

For summer in Figure 18b, the dipole structure typical for Rex blocks is clearly visible. Each combination of size and propagation velocity had a warm core around the centre of the block, and a cold core to its south.

	0%	20%	40%	60%	80%	100%
Size(km^2)						
Winter	202448	935461	1264802	1589614	2045668	8348704
Summer	195156	647272	833450	1028276	1316796	5513722
Velocity(km/day)						
Winter	−1718	−121	42	168	317	1709
Summer	−1709	−75	38	133	249	2031

Table 2: Blocking sizes and propagation velocities for different percentiles in winter and summer.

Just as in winter, the temperature anomalies get stronger for larger blocks, although this seems to primarily affect the warm core. For the same size but different velocities, the temperature anomaly pattern barely changes, which is what we expected based on the faster warming mechanism in summer. The only notable change is a zonal shift of the dipole with respect to the blocking centre. For westward-moving blocks the dipole is located at the blocking centre, while for the fastest eastward-moving blocks the dipole is located more on the west-side of the block. Not only the location of the dipole as a whole changes, but it also tilts more towards the east for westward-moving blocks and towards the west for eastward-moving blocks. For both directions, the warm core is thus located on the upstream side of the block as a result of the warming that has already taken place there.

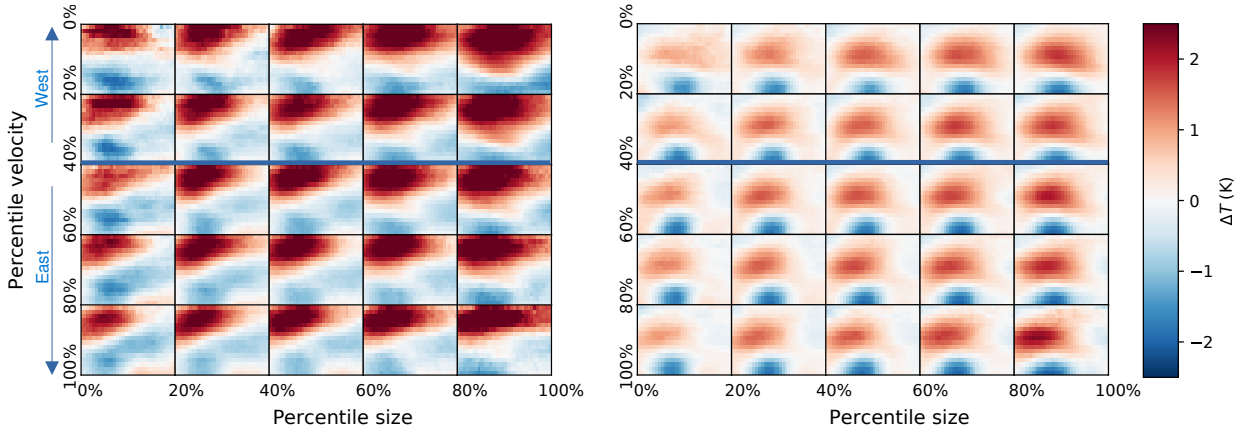

(a) DJF (b) JJA

Figure 19: As in Figure 18, but for the 2m temperature anomalies over land only.

When we limit the temperature anomaly data-points to those over land only, we end up with Figure 19. In line with our findings in Section 3.3.1, the temperature anomalies for both winter and summer are larger compared to the temperature anomalies over both land and ocean. In terms of the change in temperature patterns, the same observations can be done as in Figure 18. For both seasons the temperature anomalies become stronger when the block becomes larger, and the different propagation velocities result in different temperature patterns in winter and a shift in the temperature pattern in summer.

In Appendix D, the same figures are shown with respect to a mean state, such that differences between the compartments are better visible.

4 Discussion

4.1 Model biases

The results in Section 3 need to be considered in light of the model accuracy and choices that were made for the blocking index. In Section 2 it was described that the ECE3p5 model was chosen as it simulates more realistic temperatures for the Northern Hemisphere compared to ECE3. In Figure 6b, the warming trend in both ERA5 and ECE3p5 could be seen for the Northern Hemisphere, where the warming trend in ECE3p5 is stronger than for ERA5. However, this trend does not seem to significantly change the model outputs of the propagation velocity of atmospheric blocking as can be seen in Appendix B. Therefore, the differences in temperature trends are probably of minimal importance for the propagation velocity, although they may be important for other blocking characteristics. At the same time, the same temperature anomaly will affect us more over a warmer than a cooler base climate, making the trend in temperature particularly important for future warming.

Temperature is also closely linked to the geopotential height. Higher temperatures lead to an expansion of the lower atmosphere and thus to a higher geopotential height (Christidis and Stott 2015). This relation between temperature and geopotential height is evident in both the model and the reanalysis data, as depicted in Appendix A, Figure 22. This observation is in line with the increasing temperatures in Figure 6b. In addition to the overestimation of the geopotential height, the model also tends to overestimate its gradients, as indicated in Figure 23. In this figure, the regions where the model underestimates the gradient of the geopotential height are identical to the regions where the model underestimates the blocking frequency in Figure 9. The correlation between the overestimation of the Z500 and the blocking frequency is less prominent, but can still be recognized. These findings suggest that the model's biases in Z500 and its gradients may contribute to its limitations in accurately representing blocking events.

Other biases that play a role in most climate models, are overestimation of the jets over the oceans (Anstey et al. 2013; Delcambre et al. 2013; Pithan et al. 2016), and misrepresentation of the orography (Narinesingh et al. 2020; Berckmans et al. 2013). Although we did not test if those biases are also incorporated in the ECE3p5 model, it is plausible to think so. Models often simulate jets to be too strong and too far land-inwards. As blocks form at the end of those jets, this results in an eastward shift of the blocking frequency in models. This same effect can be seen for the winter simulations of ECE3p5 in Figure 9 and 10, where the model underestimates the amount of blocks over the Atlantic and the Pacific, while there is an overestimation over Russia and Alaska. The orography plays an important role in mountainous areas, such as the Ural and Alaska. These regions both show a negative bias in the amount of simulated blocks by ECE3p5.

4.2 Choice of blocking index

As discussed in Section 2.3.2, there are many differences in the blocking indices used by researchers. These differences in the definition and calculation of blocking indices can have implications for the outcomes of our study. Here, we will examine some of these discrepancies and how they may affect our results.

One significant modification we made compared to the method proposed by Sousa, Barriopedro, et al. (2021) was the redefinition of the minimum blocking latitude, as depicted in Figure 8. This adjustment of the minimum blocking latitude resulted in a mean poleward shift over the Atlantic and a mean equatorward shift over the Pacific ocean. These shifts have implications for the identification and measurement of blocking events. When we use their fixed minimum latitude, we get the blocking frequency as shown in Figure 20, where indeed more ridges are captured than in Figure 9. Consequently, this divergence also impacts the outcomes presented in Figure 15. Using the more static minimum latitude of Sousa, Barriopedro, et al. (2021) leads to Figure 21. In this figure, the blocks appear to be concentrated along the minimum latitude, particularly during the summer season. This shows the extent in which our results are influenced by the chosen minimum blocking latitude.

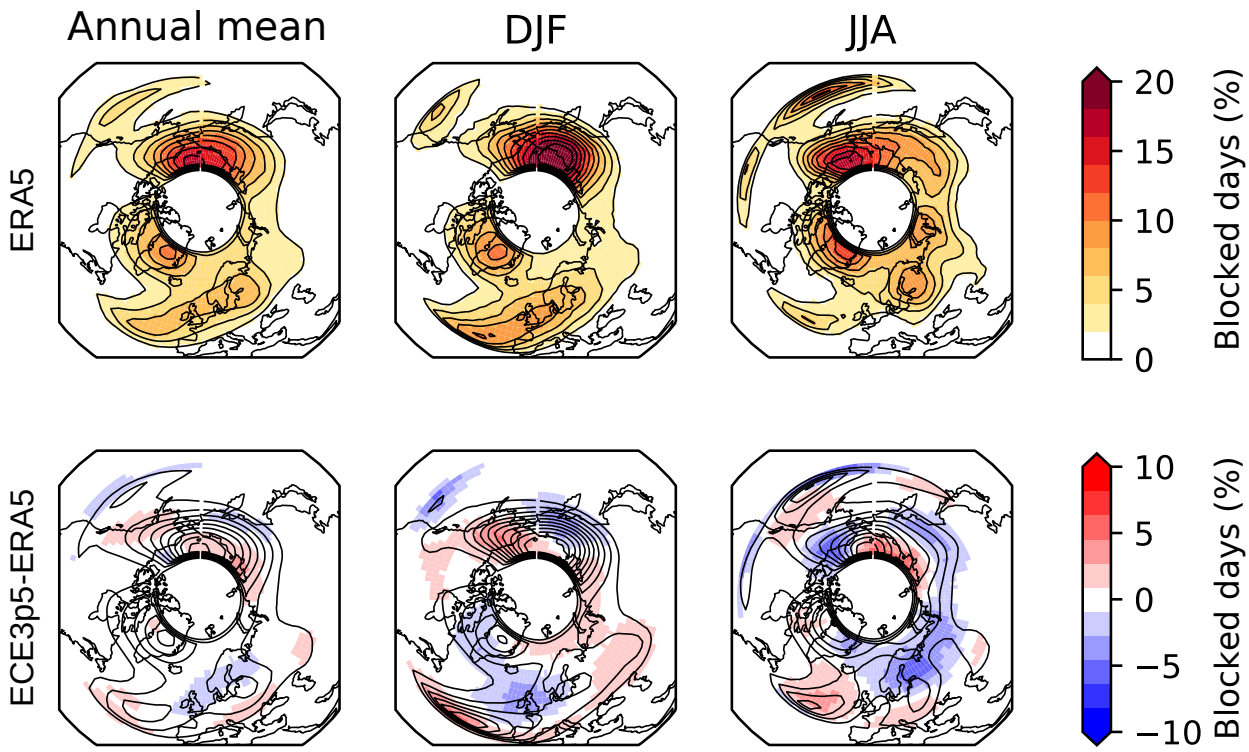

Figure 20: As in Figure 9, but for the minimum blocking latitude of Sousa, Barriopedro, et al. (2021).

Some studies employ a second geopotential height gradient to further refine the selection of blocking events. This additional gradient,

$$\mathrm{GHGS}_2(\lambda, \phi, d) = \frac{[Z500(\lambda, \phi - \Delta\phi, d) - Z500(\lambda, \phi - 2\Delta\phi, d)]}{\Delta\phi}, \tag{4.1}$$

is also used by Sousa, Barriopedro, et al. (2021), but they use it solely to differentiate between Rex blocks and Omega blocks. Keeping the additional gradient would thus lead to a loss of all blocks that do not have the strong flow reversal underneath the block, such as omega blocks and ridges. This additional gradient is also used by Davini and d'Andrea (2020). The results that Davini and d'Andrea (2020) get for their blocking frequencies resembles our result in Figure 9, even though they used a fixed minimum latitude of 30°N. Their use of GHGS_2, which restricts their blocks mostly to Rex blocks that are found at higher latitudes, presumably allows for the use of a lower and fixed minimum latitude. Additionally, the choice of threshold values for the geopotential height gradients (GHGS and GHGN) within the blocking index can also have a significant impact. Sousa, Barriopedro, et al. (2021) set the threshold values of GHGN and GHGS to 0 m/deg, whereas Davini and d'Andrea (2020) uses GHGN< -10 m/deg. The higher value for GHGN used by Sousa, Barriopedro, et al. (2021) ensures the inclusion of more local reversals, which would otherwise have been excluded.

In our study, we made the decision to follow the choices made by Sousa, Barriopedro, et al. (2021) to include all types of blocking events, rather than distinguishing between them. As the propagation velocity of blocks is assessed by the initial and final location of the blocking centre, we have only one value of the propagation velocity per block. Blocking events can however change shape over their lifetime. In the analysis of Sousa, Barriopedro, et al. (2021), it was found that blocks often start off as ridges, develop into omega blocks, and can end up as Rex blocks. This makes it hard to classify a block as either an omega block or a Rex block, which is why we decided to not make this distinction. For future research, it may be relevant to make this differentiation and relate it to the propagation velocity, to see if different kinds of blocks inherit different propagation velocities.

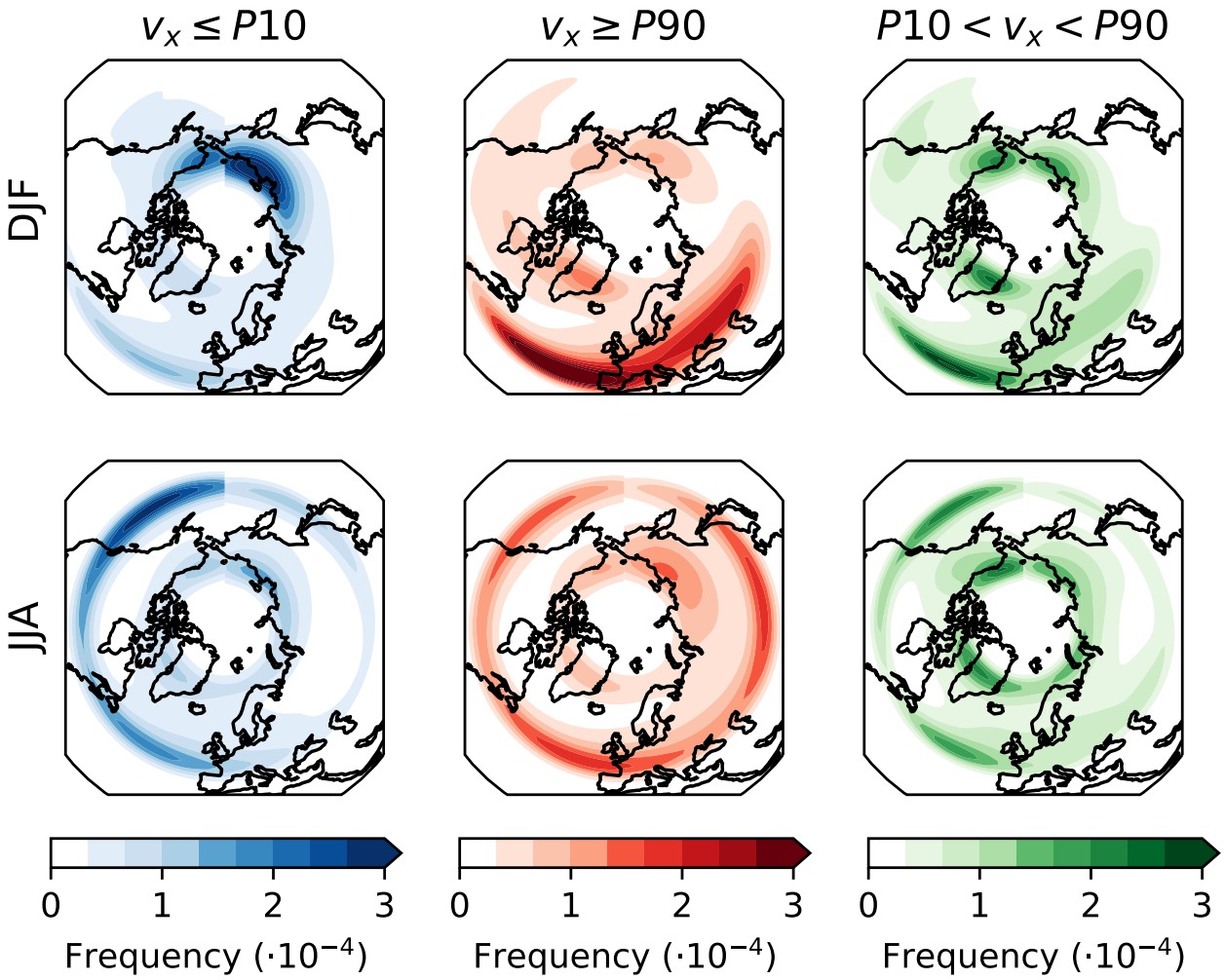

Figure 21: As in Figure 15, but for the minimum blocking latitude of Sousa, Barriopedro, et al. (2021).

A last important aspect of our study is the utilization of blocking centres, which are tracked using the 2D celltracking algorithm. As outlined in Section 2.4.2, the blocking centre is determined by weighting the blocking intensity. Considering our minimum blocking area of 500000 km^2, the blocking centre has the potential to move a considerable distance while remaining within the boundaries of the blocked area. Despite this, we opted to work with the weighted centre rather than an unweighted centre due to the association of higher intensities with greater impacts. As some of the blocks had long tails with a very low intensity, the unweighted centre would have trailed too far away from the area that is impacted by the blocks.

4.3 Other simplifications

Our study involves more simplifications that may impact the analysis and results. One notable simplification is the treatment of all blocks as equal events, despite their spatial variations, as demonstrated in Figure 15. Blocks occurring at different locations can lead to varying impacts due to factors such as orography, orientation to large water bodies, and latitude, all of which can influence the temperature and humidity of the advected air. While we attempt to compensate for this simplification by separating blocks over land and over oceans, a lot of details will be lost due to the generalization.

Another simplification we made is the focus on winter and summer months. This decision is based on the distinct characteristics of blocks during these seasons, and they are also the most studied in literature.

However, it is important to recognize that even within these seasons, there are variations that are averaged out when analyzing on a seasonal basis, as illustrated in Figure 12. The transitional character of spring and autumn makes these seasons more of a challenge to assess. As Brunner, Hegerl, and Steiner (2017) found, the average relation between blocks and their temperature impacts changes during spring, which makes it even more interesting for research in a warming world.

Lastly, the choice to work with a Lagrangian framework for studying the temperature influences of blocking events is not immediately intuitive, especially not when you are interested in the weather directly overhead. However, this approach does offer valuable new insights into how blocking events leads to different temperature anomalies, and into which factors contribute to them. It also reveals that the impact of a block is not confined solely to the region directly underneath stationary blocks, as faster moving blocks leave their trace of temperature anomalies as well. Generally, we can thus expect a faster moving block to impact any region that it will cross in the near future. To obtain a more comprehensive picture, it would be beneficial to project the Lagrangian temperature profiles to specific areas of interest. This would enable a better understanding of how blocks, whether they are slowly travelling or stationary, influence temperature patterns in those regions. By integrating the local-scale projections, we would be able to use both the advantages of a Lagrangian framework and the practical implications for local weather conditions.

5 Conclusion

In conclusion, this study aims to advance our understanding of the propagation velocity of atmospheric blocking and its influence on temperature anomalies at the Earth's surface. Atmospheric blocking has been extensively studied since the 1950's (Rex 1950a), with a lot of focus on its frequency and impact on our weather in different seasons (Kautz, Martius, et al. 2022). However, the propagation velocity of atmospheric blocking has been largely overlooked, primarily due to the general quasi-stationary nature of blocks and the predominant use of Eulerian framework in their analysis. Previous studies that did consider the propagation velocity treated it as a secondary aspect, without delving into its significance (Sumner 1963; Steinfeld et al. 2018; Mokhov and Timazhev 2019). Steinfeld et al. (2018) concluded its study on blocking propagation by mentioning that some blocks portrayed larger propagation velocities of 10 m s^{-1} (864 km/day), but that perhaps they could not be seen as classical blocks.

To address this research gap, this study adopts a Lagrangian perspective to gain deeper insights into the dynamics of atmospheric blocks. By combining the blocking index of Sousa, Barriopedro, et al. (2021), the blocking intensity of Wiedenmann et al. (2002), and the celltracking algorithm of Lochbihler, Lenderink, and Siebesma (2017), together with some alternations where needed, we employ a unique methodology to identify and track the blocks. With this combination of methods, we evaluate the performance of the EC-Earth3$_{p5}$ climate model compared to ERA5 reanalysis data, examine the seasonality of the zonal propagation velocity and its interplay with other blocking attributes, and investigate the influence of the propagation velocity on temperature anomalies in comparison to blocking size.

The evaluation of the model performance reveals differences in the spatial distribution of blocking frequencies between ERA5 and ECE3p5. Especially in summer, ECE3p5 underestimates the amounts of blocks over large regions in the Northern Hemisphere, such as over Scandinavia, Alaska, and parts of Russia. This underestimation over Europe is a well-known limitation of climate models (Woollings et al. 2018). Incorporating blocking intensity further amplifies the discrepancies between the model and reanalysis data. However, when considering frequency, size, duration, intensity and propagation velocity collectively, the only significant difference between ERA5 and ECE3p5 was observed in the summer frequency. No large differences are found between the 16 ensemble members of ECE3p5, meaning that the model does not portray a large intramodel variability within the time span of 1850-2014.

After the evaluation of the ECE3p5 model, we examine the characteristics of atmospheric blocks, focused on their seasonality, and explore relationships between different blocking aspects. Our findings reveal a wide range of propagation velocities, spanning from -1500 km/day to +1500 km/day, as determined by our blocking index. These values surpass those reported by Steinfeld et al. (2018), who questioned the classification of blocks exhibiting similar velocities. Additionally, we identify seasonality in the size, the duration, the blocking intensity, and the propagation velocity, with duration showing the least pronounced seasonal variation and the others exhibiting clearer patterns. The size, intensity, and propagation velocity exhibit their minimum values in summer, albeit with some phase-shifts among them, while the duration reached its maximum during this season.

Another noteworthy discovery is the disparity in behaviour between eastward-moving blocks and westward-moving blocks. On a seasonal basis, westward-moving blocks display larger sizes and a more linear relationship between size and velocity compared to the eastward-moving blocks. This quasi-linear relationship between westward-moving blocks and the size is consistent when considering all blocks instead of their seasonal mean. The observed relationship resembles Rossby wave theory, wherein the largest blocks associated with westward propagation velocities, while smaller blocks tend to exhibit eastward propagation velocities. In contrast, the duration and intensity have their maximum for quasi-stationary blocks. Furthermore, we find that the fastest westward-moving and eastward-moving blocks occupied distinct locations compared to the majority of the blocks, and that these locations also varied across seasons. In winter, the fastest eastward-moving blocks are predominantly found over Greenland and stretching from Eastern Europe into Russia, while in summer, they are located over Siberia. The fastest westward-moving blocks are situated over Siberia in both winter and summer.

Investigating the influence of the propagation velocity on surface temperature anomalies, we find that temperature anomalies are more pronounced over land than over the ocean in both winter and summer, attributed to the higher heat content of the oceans. Temperature anomalies are also found to be larger in winter than in summer. This could partly be attributed to the use of daily mean temperatures, which are tempered in summer due to lower values at cloud-free nights, and to the already warmer continent in summer, leading to smaller anomalies. In winter, the coldest temperatures are associated with quasi-stationary blocks, while the warmest temperatures are associated with westward-moving blocks. On the contrary, no clear relations are found during the summer. This can be explained by the different warming and cooling mechanisms in winter and summer, which are slower in winter and thus require more time to create larger temperature anomalies, while their effect is almost immediate in summer. As we find that even the faster propagation velocities contribute to temperature anomalies, indicating that there is no need to exclude blocks from blocking analyses regarding temperature anomalies, and thus no velocity limit has to be implemented in the blocking index.

Upon categorising the blocks according to their size and propagation velocity, we observe distinct temperature patterns during winter and summer. In winter, the composite mean of all blocks exhibits warmer temperature anomalies to the northwest of the block and colder temperature anomalies to the southeast. In summer, the composite mean reveals warmer temperature anomalies beneath the block and colder temperature anomalies to its south. Comparing these patterns to the mean state of the blocks, we find that larger blocks induced more intense temperature anomalies, while smaller blocks resulted in less pronounced temperature anomalies. The propagation velocity plays a role in determining the temperature anomaly patterns. In winter, faster eastward-moving blocks lead to more confined warm anomalies, and faster westward-moving blocks to a larger spread of warm anomalies. In summer, the size have the same effect as in winter, but the propagation velocity only influence the location of the warm and cold anomalies relative to the block. Temperature anomalies for faster eastward-moving blocks are situated to the left of the block, while for faster westward-moving blocks, they appear to the right. In both cases, the largest temperature anomalies are observed upstream of the block, where the block already had the opportunity to warm the surface area below it.

For future work, it would be interesting to investigate this subject further on a more localised scale to discern regional differences more effectively. Additionally, exploring how the propagation velocity may change under global warming and its potential implications for temperature anomalies would be of great interest. In particular, the decrease in the land-sea contrast in winter and the increase in summer may be worth further investigation. Understanding these dynamics could enhance our understanding of the evolving impacts of atmospheric blocking in a changing climate.

Acknowledgements

This thesis has not been a one-persons effort, but has been made possible with the help of many people. First and foremost, I want to thank my daily supervisor at the KNMI, Hylke de Vries. Thank you for the weekly meetings in which we could discuss everything for this thesis, for all the weather and sports related chats outside of the meetings, and even the occasional lunch-run. It made it very easy to settle at the KNMI and make the necessary progress in this thesis. I am also grateful for the opportunity to present this work in the Large Scale Atmospheric Dynamics meeting in Wageningen and in one of the weekly science talks of the KNMI. This allowed me to practice my presentation and get questions and feedback from many people with a much larger background in atmospheric dynamics than I have.

I also want to thank Michiel Baatsen and Aarnout van Delden, my first and second supervisors from IMAU. The biweekly meetings with the atmospheric dynamics group were a really helpful way to share knowledge between the students and you, and gave me a lot of input and inspiration for my own work. Besides these biweekly meetings, your feedback in our meetings helped me to better interpret the results and reorganise my own thoughts and figures. Lastly, thank you for all the courses during the Climate Physics master which led me to be well prepared for this work.

Lastly, I want to show my gratitude to my fellow master students, everyone I had lunch with at the KNMI, Titus, my family, and friends for making this graduation project a pleasure, and I am glad that I can keep in touch with many of you while I will continue my scientific career by starting a PhD at the Physical Geography department in Utrecht.

A Annual mean Z500

This appendix shows some additional information on the geopotential height as simulated by the ECE3p5 climate model. In Figure 22, the annual Z500 bias of ECE3p5 compared to ERA5 reanalysis data is shown, and in Figure 23, the spatial bias in the geopotential height gradient is shown.

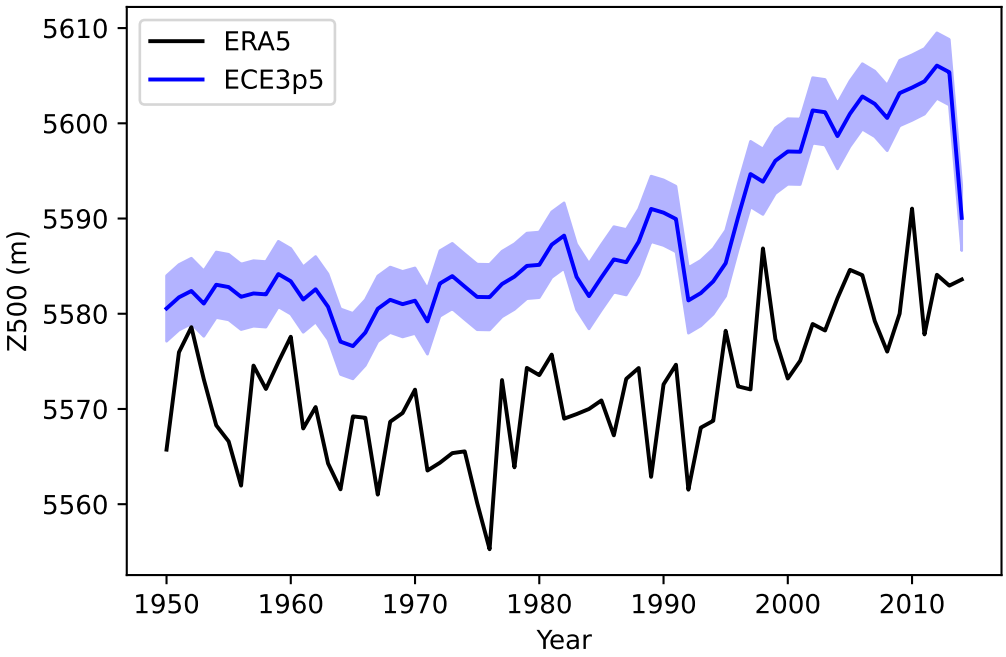

Figure 22: NH annual mean Z500 (m) for ERA5 (black) and ECE3p5 (blue) over the period of 1950-2014. Blue shading represents one standard deviation (σ) of the 16 ensemble variability.

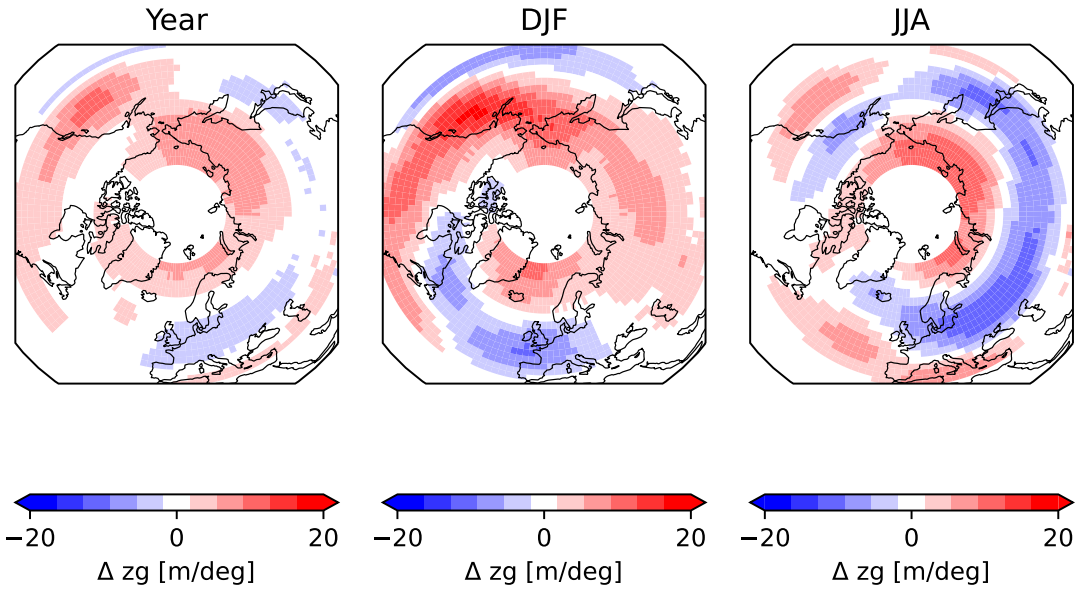

Figure 23: Difference between the gradient in Z500 for ECE3p5 and ERA5 over the period of 1951-2014 over all 16 ensemble members. Red is overestimation by the model, blue is underestimation by the model.

B Seasonality of the propagation velocity over the years

In this appendix, a timeslide of the seasonality of the absolute propagation velocity is shown over the years in Figure 24. From this figure we can see that there are no clear changes in the propagation velocity over the time period of 1850-2014 over all 16 ensembles, and thus it feels save to use the whole dataset in our analysis.

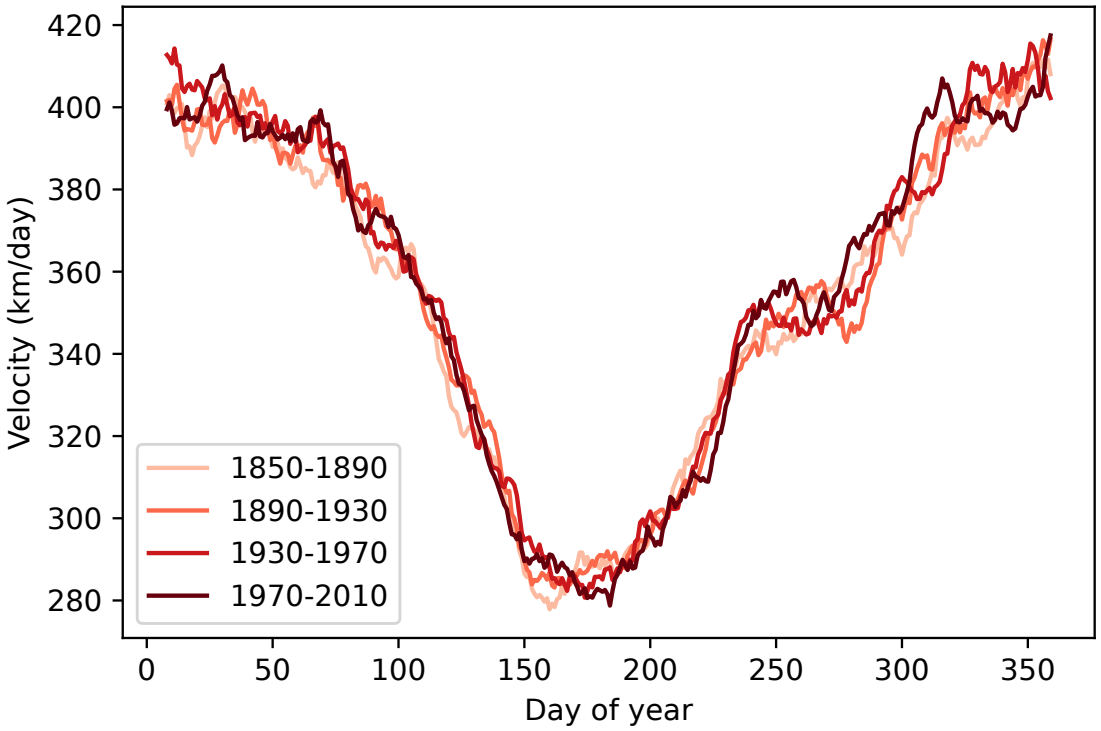

Figure 24: Timeslide of the absolute mean propagation velocity per day of the year for the ECE3p5 dataset from 1850-2014 over all 16 ensemble members.

C Temperature anomalies associated with the propagation velocity

In this appendix, the other three quadrants are included that are not discussed in Section 3.3.1.

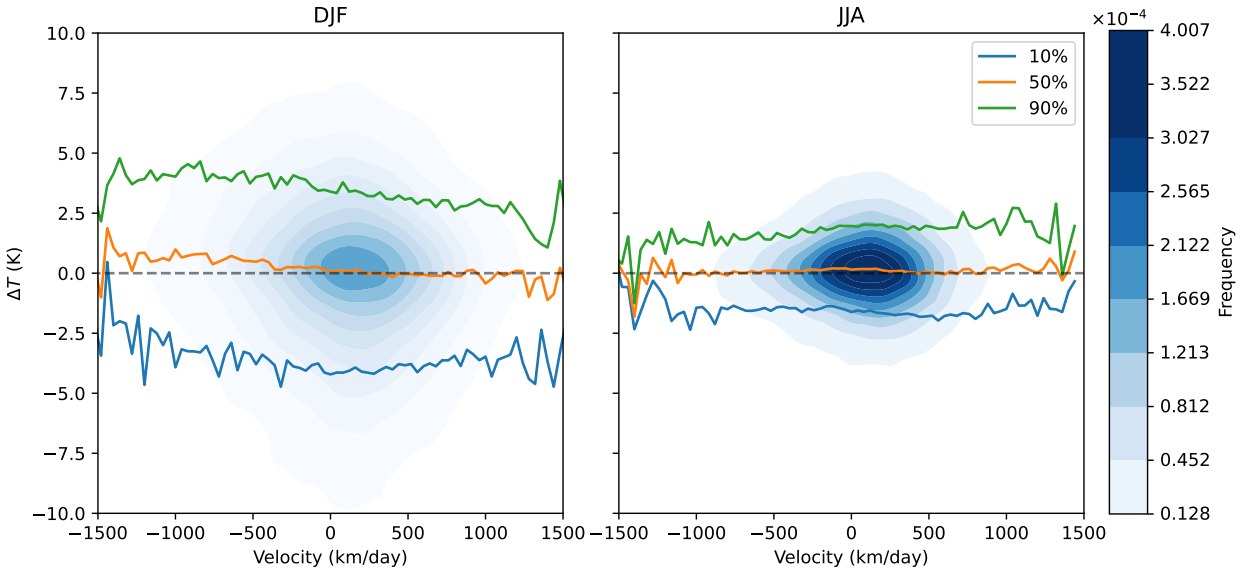

Figure 25: As in Figure 16, taken over land and ocean for the lower-left quadrant.

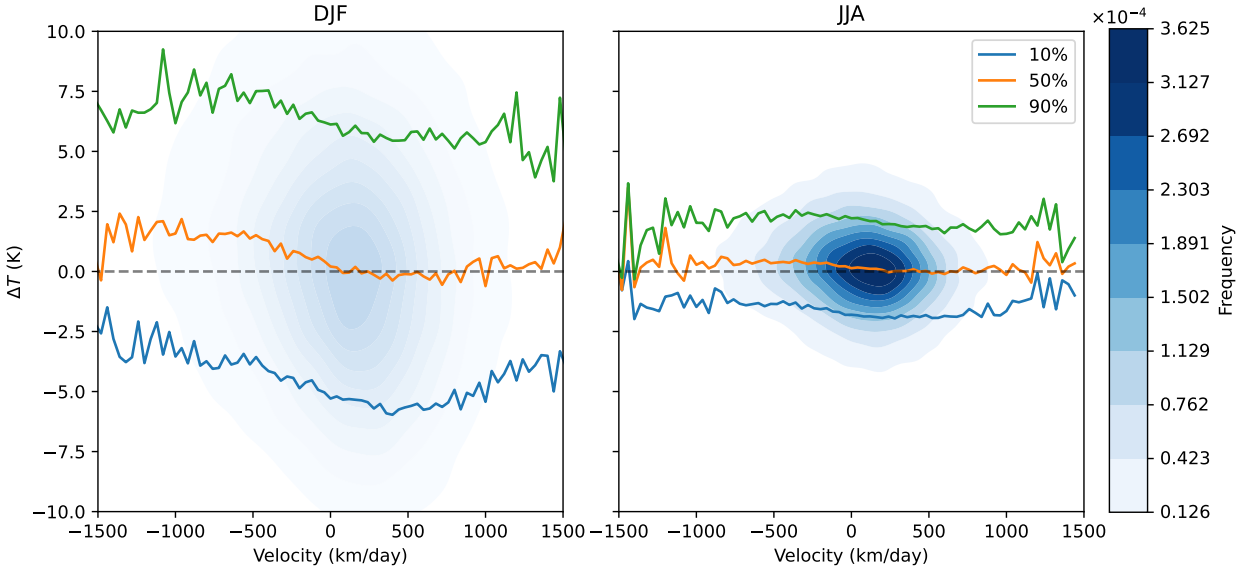

Figure 26: As in Figure 16, taken over land and ocean for the upper-right quadrant.

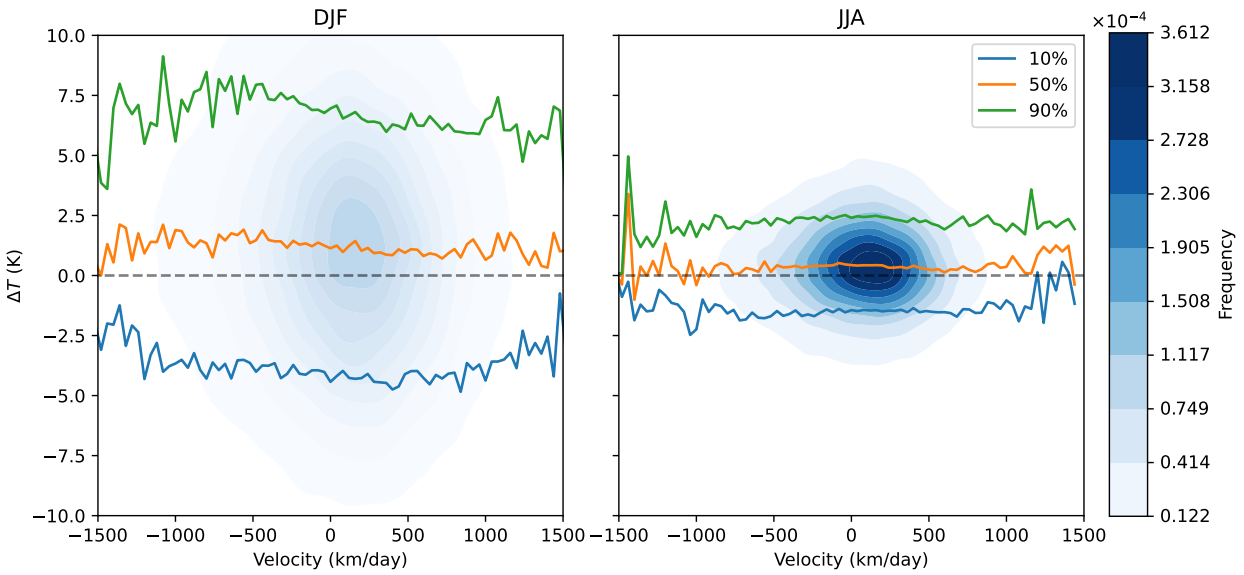

Figure 27: As in Figure 16, taken over land and ocean for the upper-left quadrant.

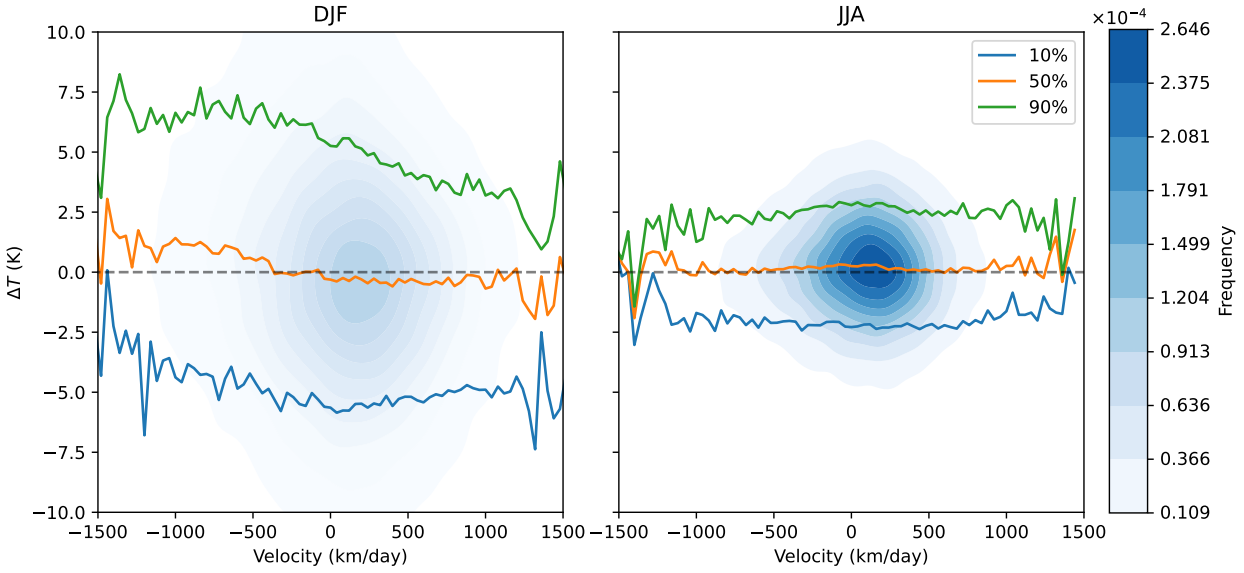

Figure 28: As in Figure 17, taken over land only for the lower-left quadrant.

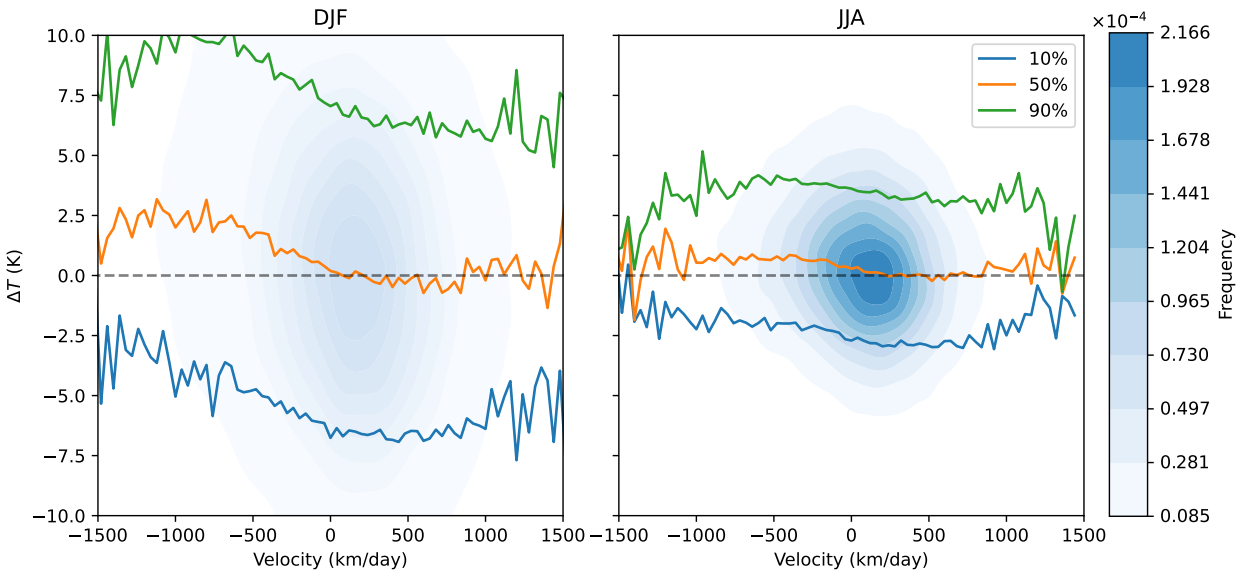

Figure 29: As in Figure 17, taken over land only for the upper-right quadrant.

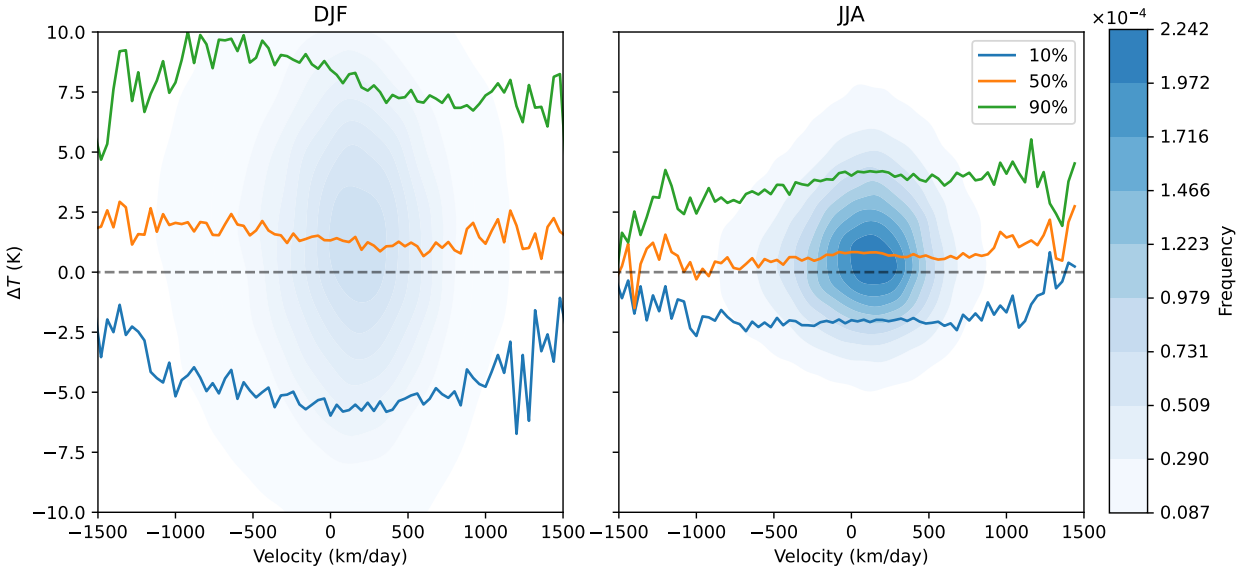

Figure 30: As in Figure 17, taken over land only for the upper-left quadrant.

D Temperature anomalies with respect to the blocking centre

In this appendix, the temperature anomalies with respect to the blocking centre are shown as deviations from the mean blocking state in Figure 31 for land and ocean, and in Figure 32 for land only. The mean blocking state is shown in the centre, between 40% and 60% for both size and propagation velocity. All other compartments show the deviation from this state.

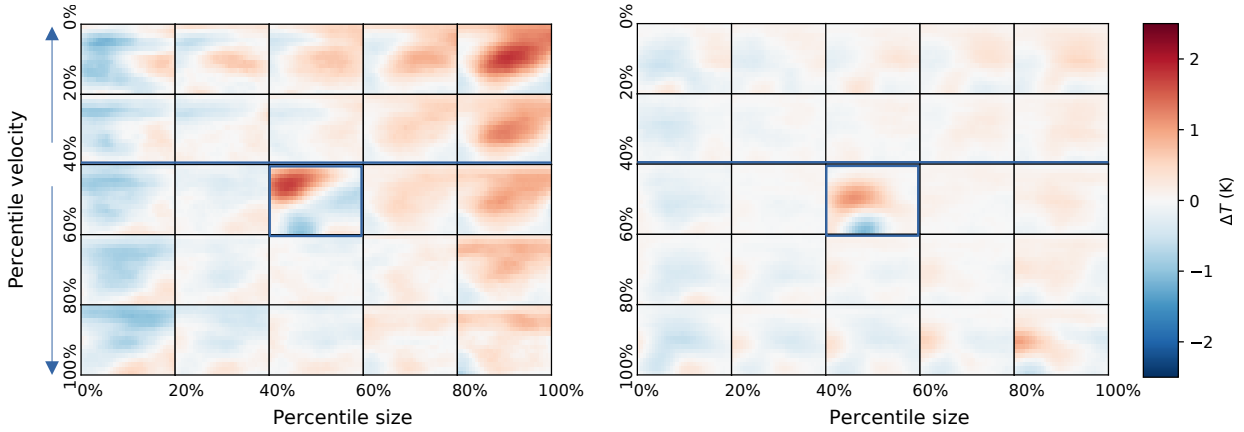

(a) DJF (b) JJA

Figure 31: Central compartment as in Figure 18, taken over land and ocean. Other compartments show the difference with respect to the central compartment.

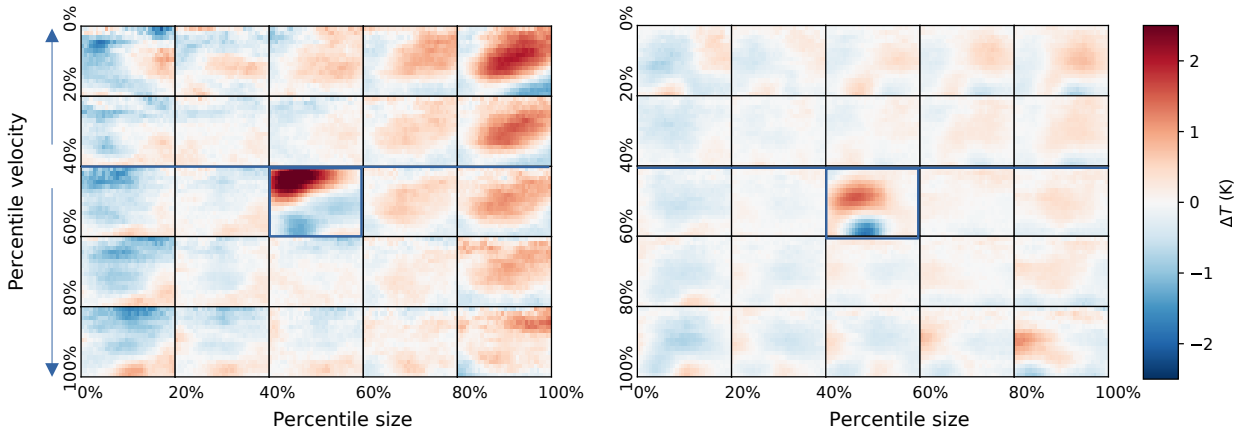

(a) DJF (b) JJA

Figure 32: Central compartment as in Figure 18, taken over land only. Other compartments show the difference with respect to the central compartment.

References

Altenhoff, Adrian M et al. (2008). "Linkage of atmospheric blocks and synoptic-scale Rossby waves: A climatological analysis". In: *Tellus A: Dynamic Meteorology and Oceanography* 60.5, pp. 1053–1063.

Anstey, James A et al. (2013). "Multi-model analysis of Northern Hemisphere winter blocking: Model biases and the role of resolution". In: *Journal of Geophysical Research: Atmospheres* 118.10, pp. 3956–3971.

Aumont, Olivier et al. (2015). "PISCES-v2: an ocean biogeochemical model for carbon and ecosystem studies". In: *Geoscientific Model Development Discussions* 8.2, pp. 1375–1509.

Balsamo, Gianpaolo et al. (2009). "A revised hydrology for the ECMWF model: Verification from field site to terrestrial water storage and impact in the Integrated Forecast System". In: *Journal of hydrometeorology* 10.3, pp. 623–643.

Barnes, Elizabeth A, Etienne Dunn-Sigouin, et al. (2014). "Exploring recent trends in Northern Hemisphere blocking". In: *Geophysical Research Letters* 41.2, pp. 638–644.

Barnes, Elizabeth A, Julia Slingo, and Tim Woollings (2012). "A methodology for the comparison of blocking climatologies across indices, models and climate scenarios". In: *Climate dynamics* 38, pp. 2467–2481.

Barriopedro, David et al. (2006). "A climatology of Northern Hemisphere blocking". In: *Journal of Climate* 19.6, pp. 1042–1063.

Berckmans, Julie et al. (2013). "Atmospheric blocking in a high resolution climate model: influences of mean state, orography and eddy forcing". In: *Atmospheric Science Letters* 14.1, pp. 34–40.

Bieli, Melanie, Stephan Pfahl, and Heini Wernli (2015). "A Lagrangian investigation of hot and cold temperature extremes in Europe". In: *Quarterly Journal of the Royal Meteorological Society* 141.686, pp. 98–108.

Brunner, Lukas, Gabriele C Hegerl, and Andrea K Steiner (2017). "Connecting atmospheric blocking to European temperature extremes in spring". In: *Journal of Climate* 30.2, pp. 585–594.

Brunner, Lukas, Nathalie Schaller, et al. (2018). "Dependence of present and future European temperature extremes on the location of atmospheric blocking". In: *Geophysical research letters* 45.12, pp. 6311–6320.

Cheung, Ho Nam, Wen Zhou, Hing Yim Mok, et al. (2013). "Revisiting the climatology of atmospheric blocking in the Northern Hemisphere". In: *Advances in Atmospheric Sciences* 30, pp. 397–410.

Cheung, Ho Nam, Wen Zhou, Yaping Shao, et al. (2013). "Observational climatology and characteristics of wintertime atmospheric blocking over Ural–Siberia". In: *Climate dynamics* 41, pp. 63–79.

Christidis, Nikolaos and Peter A Stott (2015). "Changes in the geopotential height at 500 hPa under the influence of external climatic forcings". In: *Geophysical Research Letters* 42.24, pp. 10–798.

Coon, MD, GA Maykut, and RS Pritchard (1974). "Modeling the pack ice as an elastic-plastic material". In.

Copernicus Climate Change Service, Climate Data Store (2023). *ERA5 hourly data on single levels from 1940 to present.* DOI: 10.24381/cds.adbb2d47.

Davini, Paolo, Chiara Cagnazzo, Silvio Gualdi, et al. (2012). "Bidimensional diagnostics, variability, and trends of Northern Hemisphere blocking". In: *Journal of Climate* 25.19, pp. 6496–6509.

Davini, Paolo, Chiara Cagnazzo, Richard Neale, et al. (2012). "Coupling between Greenland blocking and the North Atlantic Oscillation pattern". In: *Geophysical Research Letters* 39.14.

Davini, Paolo and Fabio d'Andrea (2020). "From CMIP3 to CMIP6: Northern Hemisphere atmospheric blocking simulation in present and future climate". In: *Journal of Climate* 33.23, pp. 10021–10038.

Delcambre, Sharon C et al. (2013). "Diagnosing Northern Hemisphere jet portrayal in 17 CMIP3 global climate models: Twenty-first-century projections". In: *Journal of Climate* 26.14, pp. 4930–4946.

Dong, Li et al. (2018). "The dynamical linkage of atmospheric blocking to drought, heatwave and urban heat island in southeastern US: A multi-scale case study". In: *Atmosphere* 9.1, p. 33.

Döscher, Ralf et al. (2022). "The EC-Earth3 earth system model for the coupled model intercomparison project 6". In: *Geoscientific Model Development* 15.7, pp. 2973–3020.

ECMWF (2010). "IFS Documentation CY36R1 - Part IV: Physical Processes". eng. In: 4. Operational implementation 26 January 2010. ECMWF. DOI: 10.21957/2loi3bxcz. URL: https://www.ecmwf.int/node/9233.

Garriott, Edward Bennett (1904). *Long-range weather forecasts.* 35. US Government Printing Office.

Guardian, The (2018). *Beast from the East meets storm Emma, causing UK's worst weather in years.* URL: https://www.theguardian.com/uk-news/2018/mar/01/beast-from-east-storm-emma-uk-worst-weather-years (visited on 03/01/2018).

Hersbach, Hans et al. (2020). "The ERA5 global reanalysis". In: *Quarterly Journal of the Royal Meteorological Society* 146.730, pp. 1999–2049.

Holton, James R. and Gregory J. Hakim (2013). "Chapter 5.7 - Atmospheric Oscillations: Linear Perturbation Theory, Rossby Waves". In: *An Introduction to Dynamic Meteorology (Fifth Edition)*. Ed. by James R. Holton and Gregory J. Hakim. Fifth Edition. Boston: Academic Press, pp. 159–165. ISBN: 978-0-12-384866-6. DOI: https://doi.org/10.1016/B978-0-12-384866-6.00005-2. URL: https://www.sciencedirect.com/science/article/pii/B9780123848666000052.

Ji, LR and S Tibaldi (1983). "Numerical simulations of a case of blocking: The effects of orography and land–sea contrast". In: *Monthly weather review* 111.10, pp. 2068–2086.

Kautz, Lisa-Ann, Olivia Martius, et al. (2022). "Atmospheric blocking and weather extremes over the Euro-Atlantic sector–a review". In: *Weather and Climate Dynamics* 3.1, pp. 305–336.

Kautz, Lisa-Ann, Inna Polichtchouk, et al. (2020). "Enhanced extended-range predictability of the 2018 late-winter Eurasian cold spell due to the stratosphere". In: *Quarterly Journal of the Royal Meteorological Society* 146.727, pp. 1040–1055.

Kawamiya, Michio et al. (2020). "Two decades of Earth system modeling with an emphasis on Model for Interdisciplinary Research on Climate (MIROC)". In: *Progress in Earth and Planetary Science* 7, pp. 1–13.

Kikuchi, Yukio (1971). "Influence of mountains and land-sea distribution on blocking action". In: *Journal of the Meteorological Society of Japan. Ser. II* 49, pp. 564–572.

KNMI (2018). *Warmste zomer in minimaal 3 eeuwen*. URL: https://www.knmi.nl/nederland-nu/klimatologie/maand-en-seizoensoverzichten/2018/zomer (visited on 09/03/2018).

Li, Muyuan et al. (2020). "Collaborative impact of the NAO and atmospheric blocking on European heatwaves, with a focus on the hot summer of 2018". In: *Environmental Research Letters* 15.11, p. 114003.

Liu, Qing (1994). "On the definition and persistence of blocking". In: *Tellus A* 46.3, pp. 286–298.

Lochbihler, Kai, Geert Lenderink, and A Pier Siebesma (2017). "The spatial extent of rainfall events and its relation to precipitation scaling". In: *Geophysical Research Letters* 44.16, pp. 8629–8636.

Lupo, Anthony R (2021). "Atmospheric blocking events: a review". In: *Annals of the New York Academy of Sciences* 1504.1, pp. 5–24.

Madec, Gurvan et al. (1997). "Ocean general circulation model reference manual". In: *Note du Pôle de modélisation*.

Mansouri Daneshvar, Mohammad Reza and Friedemann T Freund (2019). "Examination of a relationship between atmospheric blocking and seismic events in the Middle East using a new seismo-climatic index". In: *Swiss Journal of Geosciences* 112.2, pp. 435–451.

Mohr, Susanna et al. (2019). "Relationship between atmospheric blocking and warm-season thunderstorms over western and central Europe". In: *Quarterly Journal of the Royal Meteorological Society* 145.724, pp. 3040–3056.

Mokhov, II and AV Timazhev (2019). "Atmospheric blocking and changes in its frequency in the 21st century simulated with the ensemble of climate models". In: *Russian Meteorology and Hydrology* 44, pp. 369–377.

Molteni, Franco et al. (2011). *The new ECMWF seasonal forecast system (System 4)*. Vol. 49. European Centre for medium-range weather forecasts Reading.

Muntjewerf, Laura et al. (2023). "The KNMI Large Ensemble Time Slice (KNMI-LENTIS)". In: *EGUsphere* 2023, pp. 1–28.

Nabizadeh, Ebrahim et al. (2019). "Size of the atmospheric blocking events: Scaling law and response to climate change". In: *Geophysical Research Letters* 46.22, pp. 13488–13499.

Nakamura, Noboru and Clare SY Huang (2018). "Atmospheric blocking as a traffic jam in the jet stream". In: *Science* 361.6397, pp. 42–47.

Narinesingh, Veeshan et al. (2020). "Atmospheric blocking in an aquaplanet and the impact of orography". In: *Weather and Climate Dynamics* 1.2, pp. 293–311.

Paris Agreement (2016). URL: https://treaties.un.org/pages/ViewDetails.aspx?src=TREATY&mtdsg_no=XXVII-7-d&chapter=27&clang=_en (visited on 03/28/2019).

Pelly, Joanna L and Brian J Hoskins (2003). "A new perspective on blocking". In: *Journal of the atmospheric sciences* 60.5, pp. 743–755.

Pfahl, Stephan et al. (2015). "Importance of latent heat release in ascending air streams for atmospheric blocking". In: *Nature Geoscience* 8.8, pp. 610–614.

Pinheiro, Marielle Cristine, Paul Aaron Ullrich, and Richard Grotjahn (2019). "Atmospheric blocking and intercomparison of objective detection methods: flow field characteristics". In: *Climate dynamics* 53, pp. 4189–4216.

Pithan, Felix et al. (2016). "Climate model biases in jet streams, blocking and storm tracks resulting from missing orographic drag". In: *Geophysical Research Letters* 43.13, pp. 7231–7240.

Platzman, George W (1968). "The Rossby wave". In: *Quarterly Journal of the Royal Meteorological Society* 94.401, pp. 225–248.

Reerink (∼ 2023-2024, Under review). "Retuning the EC-Earth CMIP6 version". In.

Rex, D.F. (1950a). "Blocking action in the middle troposphere and its effect upon regional climate. I. An aerological study of blocking." In: *Tellus* 2, pp. 196–211.

– (1950b). "Blocking action in the middle troposphere and its effect upon regional climate. II. The climatology of blocking action." In: *Tellus* 2, pp. 275–301.

Röthlisberger, Matthias and Olivia Martius (2019). "Quantifying the local effect of Northern Hemisphere atmospheric blocks on the persistence of summer hot and dry spells". In: *Geophysical Research Letters* 46.16, pp. 10101–10111.

Rousset, Clément et al. (2015). "The Louvain-La-Neuve sea ice model LIM3. 6: global and regional capabilities". In: *Geoscientific Model Development* 8.10, pp. 2991–3005.

Sabine, Christopher L et al. (2004). "Current status and past trends of the global carbon cycle". In: *Scope-scientific committee on problems of the environment international council of scientific unions* 62, pp. 17–44.

Scaife, Adam A et al. (2010). "Atmospheric blocking and mean biases in climate models". In: *Journal of Climate* 23.23, pp. 6143–6152.

Schumacher, Dominik L et al. (2019). "Amplification of mega-heatwaves through heat torrents fuelled by upwind drought". In: *Nature Geoscience* 12.9, pp. 712–717.

Sousa, Pedro M, David Barriopedro, et al. (2021). "A new combined detection algorithm for blocking and subtropical ridges". In: *Journal of Climate* 34.18, pp. 7735–7758.

Sousa, Pedro M, Ricardo M Trigo, et al. (2017). "Responses of European precipitation distributions and regimes to different blocking locations". In: *Climate dynamics* 48, pp. 1141–1160.

Steinfeld, Daniel et al. (2018). "The sensitivity of atmospheric blocking to changes in latent heating". In: *EGU General Assembly Conference Abstracts*, p. 2975.

– (2020). "The sensitivity of atmospheric blocking to upstream latent heating–numerical experiments". In: *Weather and Climate Dynamics* 1.2, pp. 405–426.

Sumner, E.J. (1963). "Blocking anticyclones in the Atlantic-European sector of the northern hemisphere". In: *Met. Mag.* 88, pp. 300–311.

Thorndike, Alan S et al. (1975). "The thickness distribution of sea ice". In: *Journal of Geophysical Research* 80.33, pp. 4501–4513.

Tibaldi, Stefano and Franco Molteni (1990). "On the operational predictability of blocking". In: *Tellus A* 42.3, pp. 343–365.

Tiedtke, M (1993). "Representation of clouds in large-scale models". In: *Monthly Weather Review* 121.11, pp. 3040–3061.

Tyrlis, E and BJ Hoskins (2008). "Aspects of a Northern Hemisphere atmospheric blocking climatology". In: *Journal of the atmospheric sciences* 65.5, pp. 1638–1652.

Wiedenmann, Jason M et al. (2002). "The climatology of blocking anticyclones for the Northern and Southern Hemispheres: Block intensity as a diagnostic". In: *Journal of climate* 15.23, pp. 3459–3473.

Woollings, Tim et al. (2018). "Blocking and its response to climate change". In: *Current climate change reports* 4, pp. 287–300.

World Meteorological Organization, WMO (2018). *July sees extreme weather with high impacts*. URL: https://public.wmo.int/en/media/news/july-sees-extreme-weather-high-impacts (visited on 08/01/2018).

Yamazaki, Akira and Hisanori Itoh (2013). "Vortex–vortex interactions for the maintenance of blocking. Part I: The selective absorption mechanism and a case study". In: *Journal of the Atmospheric Sciences* 70.3, pp. 725–742.